Available online at www.sciencedirect.com

ScienceDirect

Advances in Space Research 77 (2026) 5493–5513

ADVANCES IN SPACE RESEARCH (a COSPAR publication)

www.elsevier.com/locate/asr

Prediction-based strategies for robust near real-time GPS signal anomaly detection on a global scale

Gerardo Allende-Alba [a,*], André Hauschild [a], Steffen Thölert [a,b], Özge Gizem Esenbuğa [a]

[a] German Aerospace Center (DLR), Münchener Str. 20, 82234 Weßling, Germany
[b] RWTH Aachen University, Chair of Navigation, Mies-van-der-Rohe-Str. 15, 52074 Aachen, Germany

Received 30 July 2025; received in revised form 7 January 2026; accepted 12 January 2026
Available online 16 January 2026

Abstract

During an anomalous signal deformation event, off-nominal distortions of signals with respect to each other are produced. This leads to abnormal receiver-dependent pseudorange biases that pose a threat for high integrity applications. The best characterization of signal deformations is obtained using high-gain antennas. However, due to their limited tracking capabilities and costly operation, they are less suitable for continuous multi-satellite monitoring. Although using the Wide Area Augmentation System (WAAS) monitor network makes it more likely to detect signal anomalies when they occur, this approach is limited to monitor only roughly half of the GPS constellation in a permanent way. This contribution presents a methodology for continuous and global GPS L1 and L2 signal quality monitoring, aimed at the early detection of anomalous signal distortions. It is based on the estimation of very high-rate (5 min samples) intra-frequency satellite differential code biases (DCB) using observations from the International GNSS Service (IGS) network. Time series of estimates are used as monitoring metrics. Detection of non-nominal estimates is done based on an unsupervised learning mixture model using results from classical, Bayesian and neural network-based autoregressive models. To quantify the confidence of detection, epoch-wise probabilities are computed using a Markov chain model. Two anomalous signal deformation events, occurred to GPS IIF SVN66 and SVN73 satellites in 2021 and 2022, respectively, were analyzed. To evaluate the effect of such events on individual signal components and observables, precise point positioning (PPP) residuals of selected IGS stations were computed. The obtained results show that the proposed methodology is suitable for the detection on a global scale in near real-time (few minutes to few hours) of such type of events. Through an early detection mechanism, the presented strategies aim at contributing to the prompt characterization of anomalous signal deformation events.

© 2026 The Author(s). Published by Elsevier B.V. on behalf of COSPAR. This is an open access article under the CC BY license (http://creativecommons.org/licenses/by/4.0/).

Keywords: GNSS signal monitoring; GPS anomalous signal deformation; Differential code biases; Near real-time anomaly detection; Autoregressive models; Unsupervised machine learning

1. Introduction

Signal deformations occur nominally as the result of imperfections in the satellite signal generation hardware. Due to the actual properties of modulation stages, filters and high-power amplifiers as well as of the L-band antenna in the transmission chain, the characteristics of chip shapes of radiated navigation signals differ from the theoretical reference (Phelts, 2001; Pagot et al., 2015; Thoelert et al., 2015). These nominal signal deformations have been extensively studied and characterized in past studies for GPS (Phelts, 2001; Mitelman et al., 2004, Phelts et al., 2009; Thoelert et al., 2015), GLONASS (Wireman et al., 2017), Galileo (Phelts and Akos, 2006; Thoelert et al., 2015) and BeiDou 3 (Thoelert et al., 2019). Signal deformations that

* Corresponding author.
E-mail addresses: gerardo.allendealba@dlr.de (G. Allende-Alba), andre.hauschild@dlr.de (A. Hauschild), steffen.thoelert@dlr.de (S. Thölert), oezge.esenbuga@dlr.de (Ö.G Esenbuğa).

https://doi.org/10.1016/j.asr.2026.01.037
0273-1177/© 2026 The Author(s). Published by Elsevier B.V. on behalf of COSPAR.
This is an open access article under the CC BY license (http://creativecommons.org/licenses/by/4.0/).

fall outside the acceptable bounds of application-dependent tolerances are known as anomalous signal distortions or evil waveforms (Phelts, 2001). After the first documented anomalous signal deformation event occurred to GPS II SVN19 in March 1993 (Edgar et al., 1999), considerable effort has been devoted to the understanding and characterization of this type of incidents (Phelts et al., 2000; Mitelman, 2005; Phelts and Akos, 2006; Thevenon et al., 2014; Shallberg et al., 2017; Vergara et al., 2020; Zhuang et al., 2020; Phelts and Walter, 2022). When these events occur, off-nominal distortions of signals with respect to each other are produced. As a consequence, during signal tracking, the shape of the autocorrelation function at a GNSS receiver is distorted from its ideal triangular shape. This results in systematic biases in the estimated pseudoranges (Phelts, 2001). The specific magnitudes of these biases depend upon the characteristics and configuration of the radio-frequency (RF) front-end (e.g. bandwidth, filters) as well as the configuration of tracking modules, particularly the correlator spacing (Wong et al., 2011; Lestarquit et al., 2012; Thoelert et al., 2015; Hauschild and Montenbruck, 2016; Vergara et al., 2020). Accordingly, even for differential applications, such systematic biases cannot be removed by corrections, as users and reference stations do not have receivers of identical characteristics and configuration (Akos et al., 2000; Phelts et al., 2000; Phelts, 2001), posing a threat for high-integrity applications (Phelts et al., 2000; Phelts and Akos, 2006; Thevenon et al., 2014; Negrinho et al., 2021).

The best characterization of signal deformations is typically obtained using measurements from high-gain antennas (Phelts et al., 2009; Wong et al., 2011; Lestarquit et al., 2012; Tholert et al., 2015, 2020). However, this approach is mostly restricted to the characterization of nominal performance of selected satellites, given the costly operation and limited capabilities of highly-directional antennas for continuous and permanent monitoring tasks. Prompt detection and characterization of an anomalous signal deformation event is thus very difficult to achieve solely through the use of high-gain antennas. On the other hand, signal quality monitoring and fault-detection are among the main functions of Ground-based and Satellite-based Augmentation Systems (GBAS and SBAS, respectively; Phelts et al. (2013); Song et al. (2020)). Recent studies have shown the use of data from monitor stations of the Wide Area Augmentation System (WAAS) to detect anomalous signal events and, together with data from a high-antenna, to characterize GPS nominal and anomalous signal deformations (Phelts and Walter, 2022; Phelts et al., 2022). However, GBAS and SBAS signal quality monitors have been specially designed and tailored to serve aviation applications within a given service area (local or regional). In the particular case of GPS, the number of satellites that can be monitored at any given time range from only a few (in the case of GBAS) to roughly half of the constellation (in the case of WAAS). In addition, the metrics under monitoring and the configured detection thresholds may not be suitable for high-integrity applications other than aviation.

This paper presents a methodology for continuous and global GPS signal quality monitoring, conceived as part of a strategy for prompt detection (using a receiver network) and characterization (using a high-gain antenna) of anomalous signal deformation events. It is based on the estimation of 5-min samples of satellite differential code biases (DCBs) using observations from the International GNSS Service (IGS) network (Johnston et al., 2017). Due to the major impact of activation/deactivation of flex power in IIR-M and IIF satellites on intra-frequency DCBs (Esenbuğa and Hauschild, 2020), leading to more complex signatures in comparison with inter-frequency DCBs, this study focuses on the analysis of L1 and L2 signals. Time series of DCB estimates are used as monitoring metrics. Detection of off-nominal/anomalous metrics is done based on a comparison with predictions obtained with autoregressive models. The applicability of the proposed approach has been tested using data from two recent anomalous signal deformation events occurred to GPS IIF SVN66 (Phelts and Walter, 2022) and SVN73 on July 2021 and September 2022, respectively.

The paper starts with a brief introduction to signal distortions and their impact on code observation biases, followed by a description and results of the scheme for estimation of very high-rate DCBs. Then, the proposed monitoring strategy is presented, including a description of the employed classical, Bayesian and neural network-based autoregressive models and the approach for model selection and training. The last section presents the obtained prediction results as well as the scheme for scoring and probability calibration using an unsupervised learning mixture model. Likewise, anomaly detection results for the two cases under analysis are presented after a discussion of the employed Markov chain model for the computation of epoch-wise probabilities of anomalous points. An analysis of residuals of precise point positioning (PPP) solutions of selected IGS stations is also presented to evaluate the effect of the analyzed events on individual signal components and observables. Finally, a discussion on the user perspective and possible impact of this type of events for high-precision and high-integrity applications is provided.

2. Signal distortions and code biases

Due to their high correlation with other variables (e.g. satellite clock offset) in the positioning model, absolute hardware-induced code or pseudorange biases cannot be unambiguously determined (Håkansson et al., 2016; Hauschild, 2017). Yet, estimates of differences between code biases can be obtained under certain model assumptions and constraints, such as a priori knowledge or joint estimation of ionospheric delays (Mannucci et al., 1998; Li et al., 2012; Montenbruck et al., 2014; Wang et al., 2016). Estimates of differential code biases (DCBs) are

sufficient for many applications, given that common offsets of the corresponding absolute biases are absorbed by other estimates in the positioning solution, such as the receiver clock error (Hegarty et al., 2005; Håkansson et al., 2016). Up to recently, strategies for DCB estimation did not account for biases caused by signal deformations (Montenbruck et al., 2014; Wang et al., 2016; Montenbruck et al., 2017). While latest studies have improved the accuracy of satellite DCB estimates by using additional calibration procedures (Gong et al., 2021; Gong et al., 2022; Lou et al., 2023), "uncorrected" DCB estimates allow an indirect observation of biases induced by signal deformations originated at the satellite. For instance, Steigenberger et al. (2019) and Esenbuğa and Hauschild (2020) have shown that high-rate DCB estimates exhibit variations due to analog signal deformations caused by the activation of flex power in GPS IIR-M and IIF satellites whereas Su and Jiao (2023b) and Wu et al. (2024) reported similar effects in BDS signals. In this vein, the methodology introduced in this contribution builds on similar strategies based on the estimation of very high-rate DCBs without explicitly parameterizing biases due to signal deformations. This section presents a description of the method for estimating very high-rate DCBs as well as the obtained estimates for the two satellites and periods under analysis.

2.1. Estimation of very high-rate DCBs

The model of a snapshot GNSS pseudorange observation of signal component ς from satellite s to receiver r, ignoring direction-dependent phase and group delays

$$P^s_{r,\varsigma} = \rho + c\left(\delta t_r - \delta t^s + b^s_{r,\varsigma}\right) + T^s_r + I^s_{r,\varsigma} + \epsilon^s_{r,\varsigma} \tag{1}$$

is expressed in terms of the geometric range ρ, satellite and receiver clock offsets δt^s and δt_r, respectively, a satellite-receiver hardware bias $cb^s_{r,\varsigma}$, tropospheric T^s_r and ionospheric $I^s_{r,\varsigma}$ delays as well as multipath errors and receiver thermal noise $\epsilon^s_{r,\varsigma}$. Differencing two pseudorange observations $P^s_{r,A}$ and $P^s_{r,B}$ of signal components ς_A and ς_B

$$P^s_{r,A} - P^s_{r,B} = c\left(b^s_{r,A} - b^s_{r,B}\right) + \left(I^s_{r,A} - I^s_{r,B}\right) + \left(\epsilon^s_{r,A} - \epsilon^s_{r,B}\right) \tag{2}$$

results in the model of a geometry-free combination, where all common terms in Eq. (1) drop out, expressed in terms of the DCB

$$d^s_{r,AB} = c\left(b^s_{r,A} - b^s_{r,B}\right) \tag{3}$$

As the present study focuses on the analysis of intra-frequency biases, the ionospheric delays in Eq. (2) cancel out, resulting in an observation model of satellite-plus-receiver DCB affected by multipath and receiver thermal noise

$$P^s_{r,AB} = d^s_{r,AB} + \epsilon^s_{r,AB} \tag{4}$$

Typically, DCB estimates with low temporal resolution (e.g. one day) are analyzed based on the assumption of stability of both satellite and receiver biases over the considered data arc (Montenbruck et al., 2014; Håkansson et al., 2016; Wang et al., 2016; Wang et al., 2020; Xiang et al., 2020; Deng et al., 2021). In studies that evaluate the impact of flex power in GPS and BDS observations, satellite DCB estimates for each arc of activation and deactivation are obtained, which have a resolution of few to several hours (Esenbuğa and Hauschild, 2020; Wu et al., 2024). Using satellite DCB estimates for a prompt detection of signal deformations calls for the computation of values with a higher temporal resolution, as some past events observed by the WAAS network exhibited sub-hour to few-hours durations (Shallberg et al., 2017). Along these lines, an estimation of DCBs with a higher rate allows to better capture dynamic changes in satellite biases due to flex power (Steigenberger et al., 2019; Su and Jiao, 2023b) and it does not require the assumption of stability of receiver DCBs over several hours, which may be not valid for all receivers and conditions (Banville and Langley, 2011; Zhang et al., 2019).

According to the employed model in conventional network-based geodetic processing, DCBs are estimated considering a linear combination of purely receiver-dependent and satellite-dependent terms (Montenbruck et al., 2017). While this model is inaccurate owing to the multiplicative properties of the transfer function in the signal generation and reception chain (Lestarquit et al., 2012; Montenbruck et al., 2014; Thoelert et al., 2015), further studies have also shown evidence that such an approach is not applicable to all receiver types (Hauschild and Montenbruck, 2016). In general, given that signal deformations vary from satellite to satellite, for any given GNSS receiver type and configuration, the corresponding induced biases have a satellite-dependency (Hauschild and Montenbruck, 2016, Gong et al., 2018). As such, the separation of DCB terms in the aforementioned model is not strictly fulfilled in reality, as it implies the estimation of one single receiver DCB term for all tracked satellites. If a network of receivers of the same group (i.e. brand/model) is used for satellite DCB estimation, where biases due to signal deformations are not explicitly accounted for, the mean bias component is absorbed by receiver DCB estimates whereas the remaining part is reflected in satellite DCB estimates (Gong et al., 2021; Lou et al., 2023). As the strategy described in this study aims at detecting the effects of induced biases of signal deformations on satellite DCB estimates, the conventional model for DCB estimation is still a suitable approximation and is likewise applied in the present work.

First, geometry-free combinations are formed with pseudorange observations of satellite s for n visible stations at observation epoch t, as per Eq. (4). In accordance to the previous discussion, the vector of geometry-free observables is modelled in terms of satellite-specific and receiver-specific DCBs

$$\begin{pmatrix} P^s_{1,AB}(t) = d^s_{AB}(t) + d_{1,AB}(t) + \epsilon^s_{1,AB}(t) \\ P^s_{2,AB}(t) = d^s_{AB}(t) + d_{2,AB}(t) + \epsilon^s_{2,AB}(t) \\ \vdots \\ P^s_{n,AB}(t) = d^s_{AB}(t) + d_{n,AB}(t) + \epsilon^s_{n,AB}(t) \end{pmatrix} \quad (5)$$

The resulting equation system to solve at each epoch t for satellite DCB $d^s_{AB}(t)$ and n receiver DCBs $(d_{1,AB}(t), d_{2,AB}(t), \cdots, d_{n,AB}(t))$ has a rank deficiency, as it is not possible to distinguish a change in the satellite bias from a common bias to all receivers (Montenbruck et al., 2014). Current DCB analyses consider a joint estimation of all satellite and receiver DCBs for a given constellation and receiver network over a given data arc (Montenbruck et al., 2014; Wang et al., 2016; Steigenberger et al., 2019; Wang et al., 2020; Xiang et al., 2020; Deng et al., 2021). In such approaches, the rank deficiency in the respective equation system is removed by specifying a datum like, for example, a zero sum or zero mean of all satellite DCBs or a fixed receiver DCB. However, given that the equation system given by Eq. (5) is to be solved at every epoch for a single satellite, such approaches are not feasible to apply. Instead, a zero-sum condition over the R receiver DCBs at epoch t is applied

$$\sum_{r=1}^{R} d_{r,AB}(t) = 0 \quad (6)$$

which also constrains to zero the mean satellite bias due to signal deformations if receivers of the same group are used for estimation. As a result, the obtained satellite DCB estimates are not affected by changes in the constellation, such as satellite commissioning, in contrast with conventional approaches (Xiang et al., 2020). Compared with more elaborate techniques for the computation of pseudo-absolute pseudorange biases, such as observable-specific signal biases, the presented strategy allows the computation of epoch-wise single-satellite bias values without requiring extra datums (Villiger et al., 2019; Wang et al., 2020; Deng et al., 2021; Su and Jiao, 2023a). Although, the resulting DCB estimates are not directly compatible with estimates obtained, e.g., from analysis centers contributing to the IGS (Johnston et al., 2017; Montenbruck et al., 2017), they are well suited for the objectives of the present study. Monitoring tasks primarily focus on analyzing changes over time and are therefore less concerned on levelling the metric under evaluation. To avoid confusion in comparisons with other studies, the estimated satellite DCBs using the approach described above are denoted as "unlevelled DCBs" or uDCB in the present work.

2.2. Estimation results

Estimates of satellite uDCBs for SVN66 and SVN73 were obtained using observations from the May-July 2021 and August-October 2022 periods, respectively, collected by the receiver network of the IGS. Using the IGS network ensures the permanent availability of globally-distributed data sources, in accordance with the characteristics of our monitoring system under development. For consistency with the assumptions for satellite uDCB estimation described above, only Septentrio PolaRx5 and PolaRx5TR receivers were considered in the present analysis. On average, around 100 and 115 stations were employed every day during the periods May-July 2021 and August-October 2022, respectively (see Fig. 1).

For each satellite under analysis, two intra-frequency uDCBs in the L1 and L2 bands were estimated. In terms of Receiver Independent Exchange (RINEX; IGS/RTCM RINEX Committee Chair (2024)) observation codes, the estimates are C1C-C1W and C2W-C2L. The former denotes biases between observations of the C/A code and semi-codeless Z-tracking of P-code in L1 band (L1 P(Y)), whereas the latter corresponds to biases between observations of the semi-codeless Z-tracking of P-code in the L2 band (L2 P(Y)) and the long pilot component of the L2C signal.

For single-epoch satellite uDCB estimation, observations with a 30 s-time resolution obtained in the RINEX3 format were used. Elevation masks of 10° and 20° were applied for C1C-C1W and C2W-C2L uDCBs, respectively, to reduce the impact of multipath (in both cases) and of the increased squaring losses in L2 semi-codeless Z-tracking at low C/N_0 (in the latter case; Woo (2000)). In addition, to improve the overall noise characteristics of estimates, average values for 5-minutes data arcs were computed.

To assess the obtained uDCB estimates, reference values with a 2 h-time resolution were obtained according to the approach of Steigenberger et al. (2019). Fig. 2 depicts the time series of reference (denoted as high-rate) and estimated (denoted as very high-rate) values for 10-days periods in May 2021 and August 2022 for satellites SVN66 and SVN73, respectively. To ease the visual inspection of Fig. 2, uDCB estimates have been sampled and shifted by biases b to match the corresponding level of reference values. Although, in general, the time patterns of reference values due to flex power can also be observed in estimates, the results for SVN66 exhibit slightly larger relative differences than the ones for SVN73. This discrepancy can be mostly attributed to the actual dynamics of code biases of each satellite.

A more direct assessment of the statistical characteristics of uDCB estimates is shown in Fig. 3, depicting the folded empirical cumulative distribution function (eCDF) of errors. For all cases, the distributions exhibit a core close to normal. For C1C-C1W estimates of both satellites, the distributions show slightly wider tails, particularly below the first decile for SVN73. Median errors of C1C-C1W and C2W-C2L estimates for both satellites showed similar

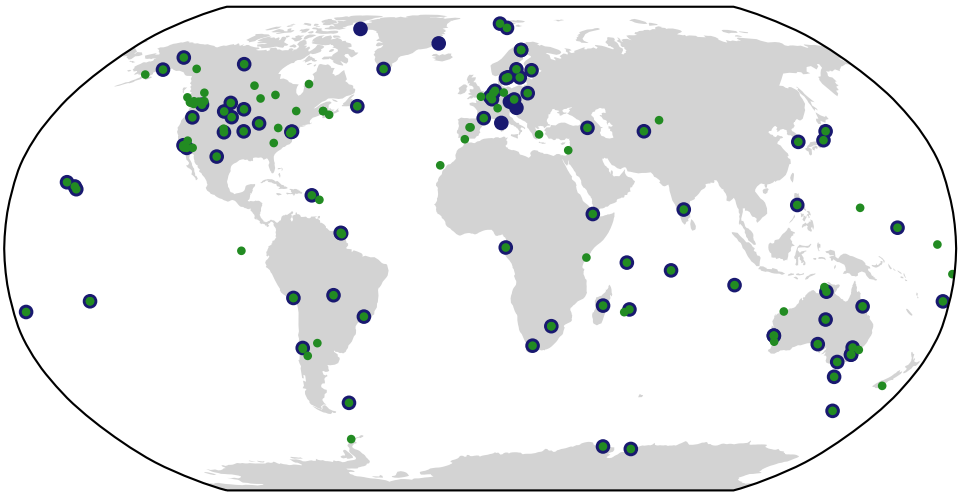


Fig. 1. Stations of the IGS network used for the analysis. Blue circles and green dots depict stations considered in the periods of 2021 and 2022, respectively.

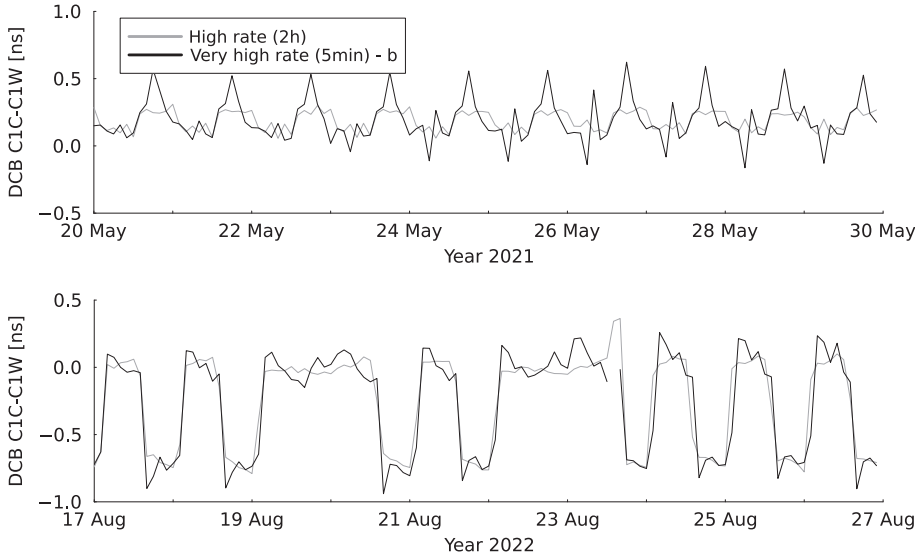


Fig. 2. Reference high-rate DCB values and very high-rate uDCB estimates in 10-days periods in May 2021 and August 2022 for satellites SVN66 (top) and SVN73 (bottom). uDCB estimates have been shifted by biases b in order to ease the visual comparison with reference values.

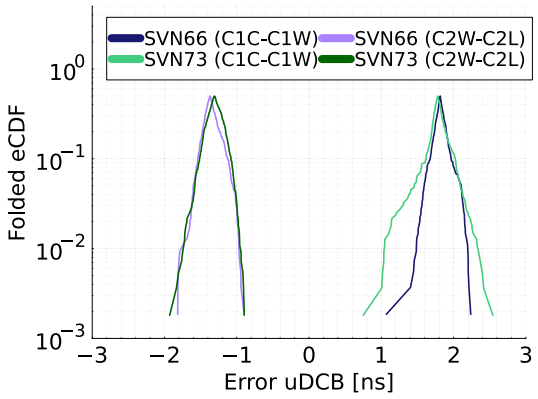


Fig. 3. Folded empirical cumulative distribution of errors of estimated uDCBs with respect to reference DCB values for satellites SVN66 and SVN73.

levels of around 1.8 ns and −1.3 ns, respectively. Overall, the estimates exhibit 1-σ errors at the 0.1–0.2 ns level.

3. Prediction-based anomaly detection

Anomaly detection is a fundamental problem in many research fields and applications (see e.g. Patcha and Park (2007) and Chandola et al. (2009) and references within). Anomaly detection in times series poses particular challenges for the development of new (and application of existing) methods due to the temporal dependency and dynamic behavior of observations, as well as due to the variety of anomaly types (Gupta et al., 2014; Blázquez-García et al., 2021; Paparrizos et al., 2022; Schmidl et al., 2022; Boniol et al., 2024). In addition, anomaly labelling is a difficult task in its own, which limits the application

and evaluation of the actual performance of supervised learning methods (Paparrizos et al., 2022; Wu and Keogh, 2023). Due to this complexity, recently-developed deep learning methods, such as convolutional, long short-term memory and transformers neural networks, have not shown until now a clear advantage over classical statistical and machine learning methods for all types of anomalies and scenarios (Audibert et al., 2022; Schmidl et al., 2022; Rewicki et al., 2023; Boniol et al., 2024; Zamanzadeh Darban et al., 2024).

Given the characteristics and expected availability of uDCB estimates used for monitoring, this study focuses on the application of autoregressive models (Hyndman and Athanasopoulos, 2021) as a part of a prediction-based unsupervised-learning anomaly detection strategy. Considering that anomalous GNSS signal deformations are very rare events (Shallberg et al., 2017; Phelts et al., 2022; Allende-Alba et al., 2024), the highly imbalanced proportion of normal and anomalous points makes the application of supervised learning difficult (He and Garcia, 2009; Fernández et al., 2018). From the various families of strategies proposed in latest years, prediction-based anomaly detection methods offer particular advantages for scenarios with streaming time series and detection of point anomalies (Blázquez-García et al., 2021; Schmidl et al., 2022; Boniol et al., 2024). Additionally, the comparative studies of Schmidl et al. (2022) and Kontopoulou et al. (2023) show that autoregressive methods still exhibit a competitive performance in some test data sets and selected applications in comparison with machine- and deep-learning based approaches. This adds up to the advantages of simplicity, less data-hungry and interpretability of classical autoregressive methods (Triebe et al., 2019). This section presents a description of the characteristics of the employed models as well as the methodology for model selection and training. Likewise, example prediction results are presented and discussed.

3.1. Model characteristics

The employed prediction strategy assumes a stream of uDCB estimates that are available at a constant rate, although missing estimates are allowed. At each epoch t of expected availability of a uDCB estimate $\widehat{d}_t^s$, a predicted value $\check{d}_t^s$ is obtained

$$\check{d}_t^s = f\left(d_{t-1}^s, d_{t-2}^s, \cdots, d_{t-\tau}^s; \widehat{\Gamma}\right) \tag{7}$$

using the prediction model f with fitted/estimated parameters $\widehat{\Gamma}$ and the τ previous values of the uDCB time series $d_{t-1}^s, d_{t-2}^s, \cdots, d_{t-\tau}^s$, where the notation $d_t^s = d_{AB}^s(t)$ has been used for simplicity, assuming implicitly signal components ς_A and ς_B. The key idea of a prediction-based strategy for anomaly detection is to compare a given data point/estimate with a prediction obtained with a model. Accordingly, as expressed by Eq. (7), the employed model must be fed with data points that resemble a nominal behavior of the time series under analysis in order to produce useful predictions. This implicit data quality control was implemented in the presented scheme through the computation of prediction intervals. For each point prediction, a prediction interval

$$\left[\Delta^-, \Delta^+\right]_{1-\alpha} = \left\{d_t^s \in \mathbb{R}, \Delta^- < d_t^s < \Delta^+\right\}_{1-\alpha} \tag{8}$$

is computed according to the employed model based on a specified coverage probability $1-\alpha$, for a tolerated error probability α. The computed prediction interval at epoch t provides a range within which an estimate $\widehat{d}_t^s$ is expected to fall with probability $1-\alpha$. In this way, it sets bounds of acceptable values that are used for a prediction at epoch $t+1$. If an estimate $\widehat{d}_t^s$ is within the computed prediction interval, it is used to feed the model, otherwise, the predicted value $\check{d}_t^s$ is employed.

Based on the characteristics of flex power activation, the observed effects in uDCB estimates (see Fig. 2) exhibit (typically) a daily seasonality (Steigenberger et al., 2019; Esenbuğa and Hauschild, 2020). Accordingly, the model f should be able to handle such seasonality to provide accurate predictions. In total, three flavors of autoregressive models were employed in this study: classical seasonal autoregressive integrated moving average (cSARIMA; Box and Jenkins (1970)), Bayesian SARIMA (BSARIMA; West and Harrison (1997)) and NeuralProphet (Triebe et al., 2021). Although none of these models are purely autoregressive, the fundamental component of each one is (as explained in the following sections), so they are referred as such for simplicity in this study. They were selected to obtain a more robust and adaptable approach for the present analysis. While SARIMA models have a long history of successful application to a diversity of problems, offering simplicity, efficiency and a competitive performance, NeuralProphet is a recently proposal that combines the interpretability of autoregressive models and the scalability of neural networks. The following sections provide a brief description of the employed models and overview of their main characteristics in the context of the prediction strategy described above is provided in Table 1.

3.1.1. Classical SARIMA

A general classical SARIMA model for a time series of uDCB values $D^s = \left\{d_t^s\right\}_{t\in T}$ is expressed as

$$\begin{aligned} f_{cS} &= \left(1-\phi_1 B - \cdots - \phi_p B^p\right)\left(1-\Phi_1 B^m - \cdots - \Phi_P B^{Pm}\right)(1-B)^i\left(1-B^m\right)^I d_t^s \\ &= \left(1+\theta_1 B + \cdots + \theta_q B^q\right)\left(1+\Theta_1 B^m + \cdots + \Theta_Q B^{Qm}\right)\varepsilon_t \end{aligned} \tag{9}$$

with model parameters $\Gamma = \left\{\phi_1, \cdots, \phi_p, \Phi_1, \cdots, \Phi_p, \theta_1, \cdots, \theta_q, \Theta_1, \cdots, \Theta_Q\right\}$ and using the backshift operator $Bd_t^s = d_{t-1}^s$. Typically, SARIMA models are referred using the notation $(p,i,q)(P,I,Q)_m$ where p denotes the order of the autoregressive part, q represents the order of the

Table 1
Overview of characteristics of prediction models.

Model	Type	Seasonality handling	Prediction interval type	Prediction interval computation
cSARIMA	Statistic	Seasonal coefficients	Parametric	Centered around predicted value
BSARIMA	Probabilistic	Posteriors of seasonal coefficients	Parametric	Central credible interval of posterior predictive
NeuralProphet	Neural network (AR-Net)	Fourier series	Non-parametric	Quantile regression

moving average part, i denotes the degree of first differencing, P, Q and I indicate the corresponding orders and degree of the seasonal part of the model and m denotes the number of data points of seasonality. While the autoregressive and moving average terms allow to model short-terms dependencies, the degrees of differencing help to capture long-term trends, both non-seasonal and seasonal. For classical SARIMA models, the computation of prediction intervals assumes that model residuals are normally distributed. For a point prediction at epoch t, the interval bounds $\Delta_t^{\pm} = \check{d}_t^s \pm k_\alpha \sigma$ are centered around the predicted values $\check{d}_t^s$, with constant k_α for coverage probability $1-\alpha$ and σ the standard deviation of residuals (Hyndman and Athanasopoulos, 2021).

3.1.2. Bayesian SARIMA

While the prediction intervals from classical SARIMA models reflect the uncertainty due to noisy observations as per the assumed distribution of residuals, they do not consider the uncertainty in the fitted model parameters. As a result, these intervals tend to be narrow (Brockwell and Davis, 2016; Hyndman and Athanasopoulos, 2021). Adapting the classical SARIMA model to a Bayesian framework allow to treat the model parameters in Eq. (9) also as i.i.d. random variables. Thus, the Bayesian SARIMA model can be written as

$$f_{BS} = \begin{cases} \boldsymbol{\Gamma} \sim \mathcal{N}(0, \sigma_\Gamma) \\ \boldsymbol{\Sigma}_d^2 \sim \mathcal{N}_{[0,\infty]}(0, \sigma_\Sigma) \\ \boldsymbol{d}_t^s \sim \mathcal{N}(\boldsymbol{\mu}_t, \boldsymbol{\Sigma}_d) \\ \boldsymbol{\mu}_t = \boldsymbol{f}_{cS}\left(\boldsymbol{d}_{t-1}^s, \boldsymbol{d}_{t-2}^s, \cdots, \boldsymbol{d}_{t-\tau}^s; \boldsymbol{\Gamma}\right) \end{cases} \tag{10}$$

where normal priors are assumed for all model parameters Γ. Similarly, the sampling distribution $\boldsymbol{d}_t^s$ is assumed normal with variance Σ_d^2 (truncated-normally distributed). For the computation of a point prediction and prediction interval at epoch t, a set of J samples $\Gamma_{j,t}$ (with $j = 1, 2, \cdots, J$) from the estimated posteriors of model parameters Γ_t is obtained. Using the functional model given by Eq. (9), a sampled posterior predictive distribution (cf. Eq. (7)) is obtained as

$$d_{j,t}^s = f_{cS}\left(d_{t-1}^s, d_{t-2}^s, \cdots, d_{t-\tau}^s; \Gamma_{j,t}\right) \tag{11}$$

A point prediction $\check{d}_t^s$ is obtained as the median of $d_{j,t}^s$ and a prediction interval is computed as the central credible interval of $d_{j,t}^s$ with coverage probability $1-\alpha$.

3.1.3. NeuralProphet

The NeuralProphet model was developed by Triebe et al. (2021) in an effort to combine the strengths of classical autoregressive models and the advantages of more recent approaches, such as neural networks and the Prophet model (Taylor and Letham, 2018). It is composed of various elements or sub-models, each one following their own modelling processes, that are combined linearly. A simplified model used in this study can be expressed as

$$f_{NP} = d_t^s = S_{\mathrm{T}}(t) + A_p(t) \tag{12}$$

where the seasonality $S_{\mathrm{T}}(t)$ with periodicity T is modelled using Fourier series and the term $A_p(t)$, accounting for autoregressive effects of order p,

$$A_p(t) = F_{\mathrm{AR-Net}}\left(d_{t-1}^s, d_{t-2}^s, \cdots, d_{t-p}^s\right) \tag{13}$$

is modelled using a modified version of the neural network AR-Net $F_{\mathrm{AR-Net}}$ proposed by Triebe et al. (2019). In its basic form, without hidden layers, AR-Net keeps the interpretability of classic autoregressive models. One particular advantage of AR-Net is its capability of scaling to large autoregressive orders, which allows to capture even very long-term effects. The corresponding prediction intervals are computed in a non-parametric way using quantile regression (Koenker and Bassett 1978). Thus, the interval bounds $\Delta_t^{\pm}$ are given by the predicted conditional quantiles $\check{d}_{t\lceil 1-\alpha/2 \rceil}^s$ and $\check{d}_{t\lceil \alpha/2 \rceil}^s$ for a coverage probability $1-\alpha$.

3.2. Model selection and training

A dataset of 7 days was selected for initial training of all models (although strictly speaking ARIMA-like models are fitted, the term *train* is used in this study for simplicity to encompass NeuralProphet as well). For cSARIMA and BSARIMA, model order selection was done also over this dataset. Due to the exhibited seasonality in uDCB estimates, a seasonal difference was applied to all estimates to obtain stationarity, resulting in degrees $i = 0$ and $I = 1$. Autocorrelation and partial autocorrelation functions were obtained and analyzed to do a first inference of autoregressive and moving average orders (Hyndman and Athanasopoulos, 2021). Based on this analysis, the final order was selected from a constrained grid search using the Akaike Information Criterion (AIC). The resulting models are listed in Table 2 for a seasonality $m = 288$ (points per day). For the case of NeuralProphet, automatic

Table 2
SARIMA models of uDCB time series with seasonality$m = 288$ used in this study.

Satellite	uDCB	Sarima model
SVN66	C1C-C1W	$(8,0,0)(0,1,1)_m$
	C2W-C2L	$(2,0,0)(1,1,1)_m$
SVN73	C1C-C1W	$(9,0,0)(0,1,1)_m$
	C2W-C2L	$(1,0,2)(1,1,1)_m$

model order selection was done, thanks to the capability of the model of handling sparse autoregressive processes (Triebe et al., 2019).

During training, model coefficients for cSARIMA were obtained using maximum likelihood estimation (Hyndman and Khandakar, 2008). For BSARIMA, posteriors of model parameters were obtained using the No-U-turn sampler extension of the Hamiltonian Monte Carlo method (Hoffman and Gelman, 2014), implemented in the Turing probabilistic programming language (Ge et al., 2018; Fjelde et al., 2025). For NeuralProphet, autoregressive coefficients were estimated using stochastic gradient descent, whereas a regularization factor was used for automatic order selection via sparse model weights (Triebe et al., 2019). For seasonality handling, eight Fourier terms of additive daily seasonality were estimated for each forecasting window (Taylor and Letham, 2018; Triebe et al., 2021).

3.3. Prediction results

The performance of trained models was tested using estimates of satellite uDCBs for SVN66 and SVN73 for the periods 20 May–2 July 2021 and 17 August–1 October 2022, respectively. For cSARIMA and BSARIMA, epochwise prediction values and intervals were obtained for each epoch of expected availability of uDCB estimates. Concerning cSARIMA models, a restart had to be applied every day using a slicing 7-day window training set with estimates below a predefined threshold, in an effort to prevent an extreme shrinkage of the prediction interval width. Given its architecture, AR-Net must be re-trained for each prediction. Thus, for the case of NeuralProphet, multi-epoch predictions were obtained in daily windows to avoid a severe computational performance degradation. Likewise, an incremental training set was used. Fig. 4 depicts a flowchart of the epochwise operation of prediction models after initial training. For all models, prediction intervals for$\alpha = 10^{-2}$ (see Eq. (8) and Table 1) were obtained.

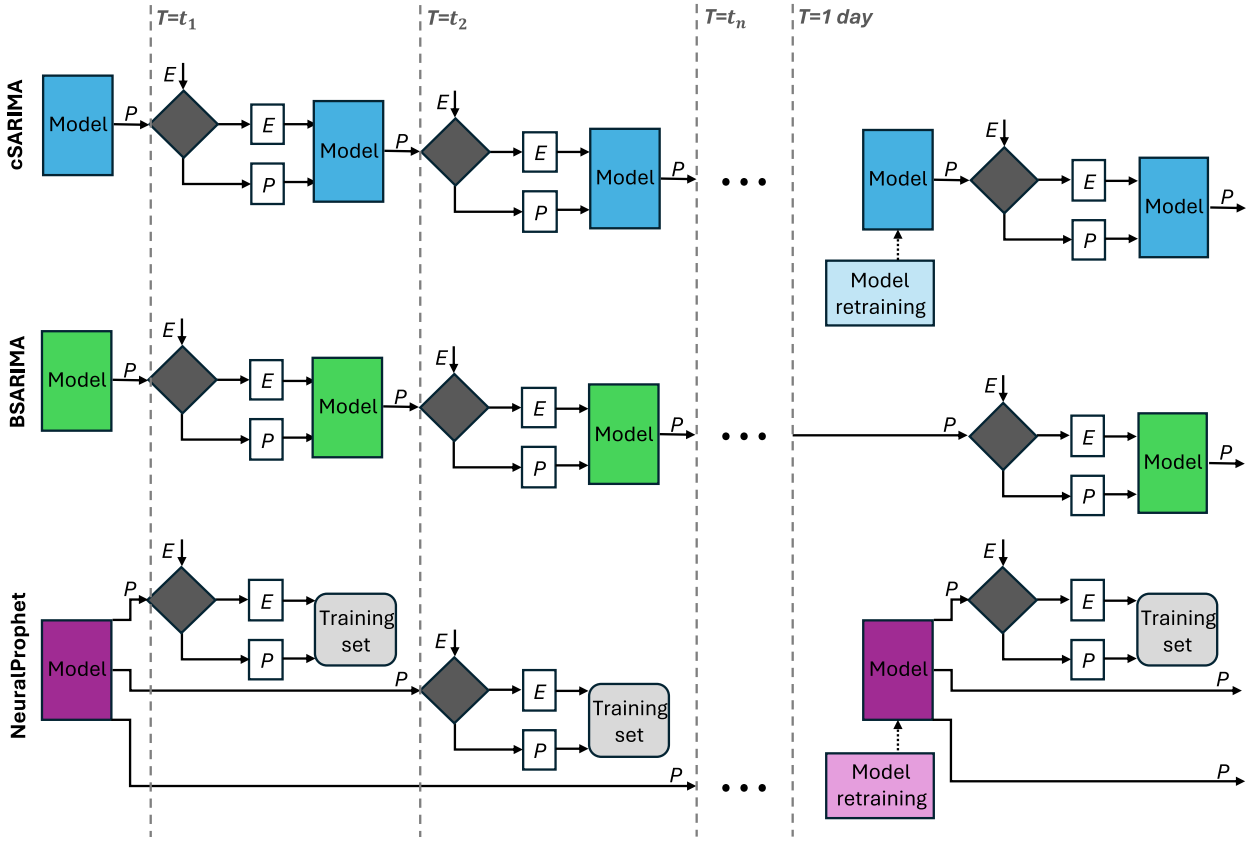


Fig. 4. Flowchart of the epochwise operation of prediction models after initial training. Decision blocks (dark gray) refer to the evaluation if the estimate (E) is within the prediction interval. If not, the predicted value (P) is used for further computations. For simplicity, data storage for cSARIMA model retraining based on a fixed threshold is not shown.

Fig. 5 shows an example of the performance of all models in comparison with estimated C1C-C1W values for SVN66 in the period 20–25 May 2021. For all cases the predicted values follow closely the estimates, highlighting the forecasting capability of the employed models. Prediction intervals from cSARIMA and BSARIMA models exhibit a smooth behavior due to their parametric determination. On the other hand, predictions from the NeuralProphet model appear slightly noisier, partially attributed to the sparsity of the model weights. Given their non-parametric determination, prediction intervals change sharply from epoch to epoch. Likewise, as the AR-Net was re-trained every day, the automatically-selected autoregressive order changed from day to day, leading to slightly different characteristics of prediction intervals on each day.

The capability of forecasting nominal states is of fundamental importance for a reliable identification of outlying points. In particular, it is essential that this characteristic is preserved in the presence of off-nominal or anomalous estimates, even for long periods. For this task, prediction intervals provide a level of certainty on the nominality of estimates through the specification of a coverage probability. As an example of models' performance, Fig. 6 depicts the estimated and predicted C1C-C1W (top) and C2W-C2L (bottom) values for SVN66 in the period 30 June-2 July 2021. According to Phelts et al. (2022), on 1 July 2021, an unintentional off-nominal configuration of L1 and L2 signals from SVN66 occurred from 11:00 to 23:00 UTC. As shown in Fig. 6, the obtained uDCB estimates in both bands show anomalous signatures during this 12-h period with respect to the previous and following day. Likewise, all models exhibit a similar performance over the depicted 3-day window, including the prediction of nominal states during the period of the reported anomaly occurrence.

The event occurred to SVN73 on 29 September 2022 has not been, to the knowledge of the authors, analyzed in detail in previous studies. The methodologies presented by Thoelert et al. (2023) and Allende-Alba et al. (2024) could detect anomalous signatures in high-rate DCB estimates occurring during the first hours of the day, whereas the WAAS network observed the anomaly partially only (Phelts, priv. comm.). Based on a visual inspection of obtained uDCB estimates for this study, it is likely that such an anomalous signal deformation event took place from the first minutes until around 12:00 of 29 September.

Fig. 7 depicts the estimated and predicted C1C-C1W values for SVN73 in the period 27–29 September 2022. In terms of predictions, other than for SVN66, the models' performance in this case is slightly different among them. Predictions from cSARIMA show several outlying points with respect to estimates. This is attributed to the strategy

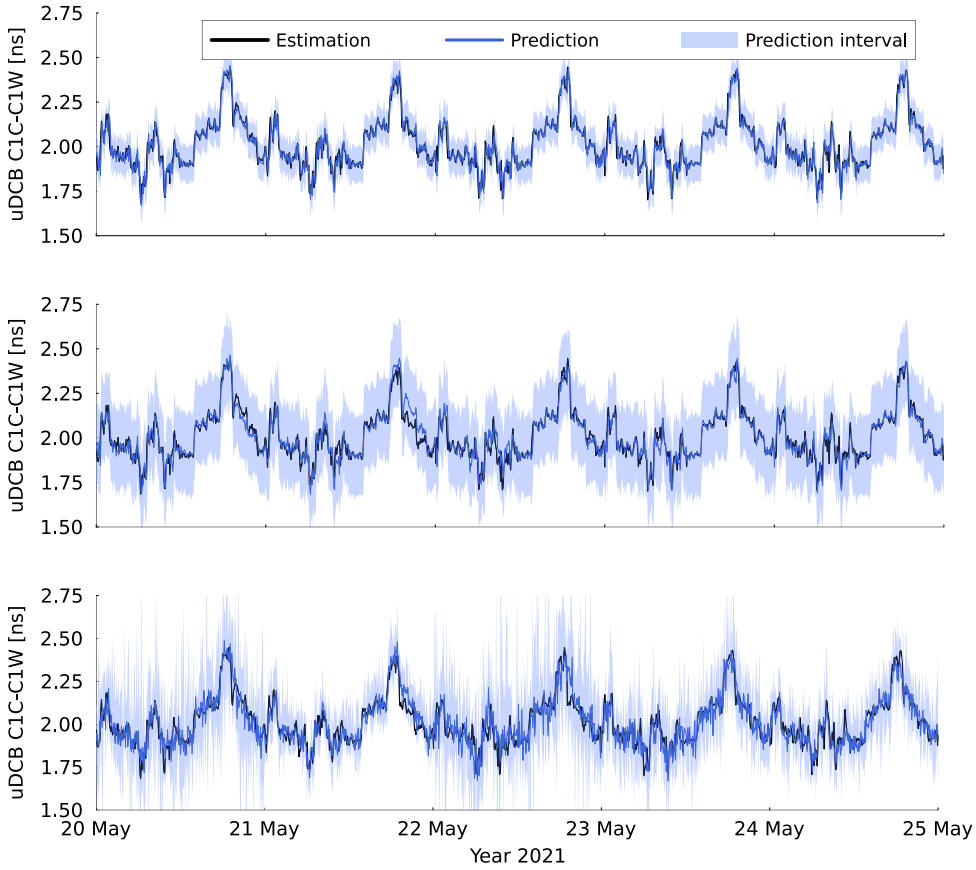


Fig. 5. Estimated and predicted C1C-C1W values and intervals for SVN66 from cSARIMA (top), BSARIMA (middle) and NeuralProphet (bottom).

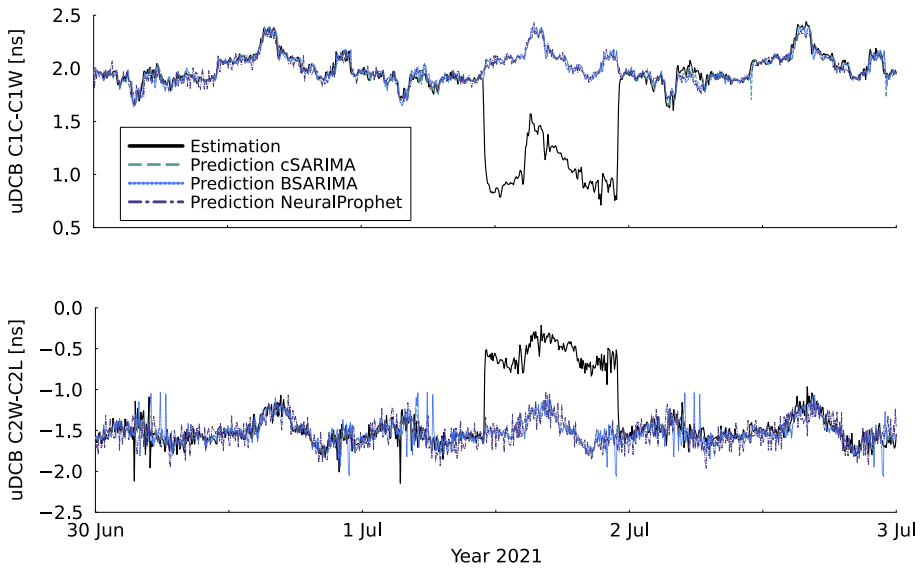


Fig. 6. Estimated and predicted C1C-C1W (top) and C2W-C2L (bottom) values for SVN66 in the period 30 June-2 July 2021.

employed to restart the model (in an effort to obtain comparable results, no fine tuning of the threshold for estimates used for model restart was done). Predictions from BSARIMA exhibit a lag with respect to estimates. Predictions from NeuralProphet show an advance with respect to estimates during the first two days of this time window, which gets slightly corrected by the third day.

The described differences in lag or lead times of predicted and estimated values are directly attributed to changes in regular patterns of estimates caused by the activation and deactivation of flex power. Since the start of its regular operation in January 2017, the activation scheme of the flex power capability of GPS IIR-M and IIF satellites has undergone several changes. While it was possible to identify stable modes during the first years (Steigenberger et al., 2019), since beginning of 2020, changes in the activation/deactivation times and regions have been more dynamic (Yang et al., 2022; Esenbuğa et al., 2023). Such changes have different effects on the employed prediction models. When no major and/or constant flex power-induced variations in uDCB estimates are present after the training phase, all models are expected to have a similar performance. Fig. 8 depicts the estimated activation/deactivation times of flex power for SVN66 (top) and SVN73 (bottom) using the algorithm of Esenbuğa et al. (2023) for the respective periods under analysis. The start and end of the corresponding initial training, holdout (used for probability calibration, as explained later) and test data sets are also indicated. For SVN66, except for a permanent activation in the period 30 May-4 June 2021, no major changes are observed in the test phase (starting on 30 May 2021). As a result, all models deliver similar predicted values in this phase, as depicted in Fig. 6. For SVN73, several changes occur in the periods of both the holdout and test sets, including phases of one to several days with permanent flex power activation (see Fig. 8). Due to the employed restart strategy, the cSARIMA model can partially adapt to these changes, at the cost producing outlying predictions for some epochs. On the other hand, as the BSARIMA model was trained using a fixed data set, its predictions mostly reflect the nominal state during such a period. Predictions from the NeuralProphet model exhibit a higher degree of adaptability, mostly due to the capabilities of the AR-Net to capture long-term dependencies.

In general, each model provides advantages for the detection of off-nominal or anomalous signatures in uDCB estimates. For the example case of SVN73, aside from the aforementioned outlying and lagged values, predictions from the cSARIMA and BSARIMA models closely resemble the falling and rising signatures in estimates when flex power activation/deactivation occur. Likewise, the higher adaptability of NeuralProphet allows predictions to tightly follow nominal estimates, even in the presence of changing patterns. To take advantage of the characteristics of all models, an ensemble solution was obtained by computing an average prediction at every epoch. The resulting solution for SVN73 in the period 27–30 September 2022, is depicted in Fig. 9. The ensemble model exhibits an improved performance with respect to the individual models in the prediction of nominal states, particularly in the period when the anomalous signal deformation event likely occurred. Accordingly, the resulting solution shows more robustness in the prediction of nominal states, even in the presence of dynamic changes in flex power activation/deactivation patterns.

The prediction results shown in Figs. 6, 7 and 9 suggest the suitability of the proposed monitoring metrics for the implementation of an anomaly detection mechanism. In general, even in the case of the same event, whether or not a given metric is labelled as anomalous, is highly dependent on the application and the architecture of the monitoring system. For example, in the case of the event

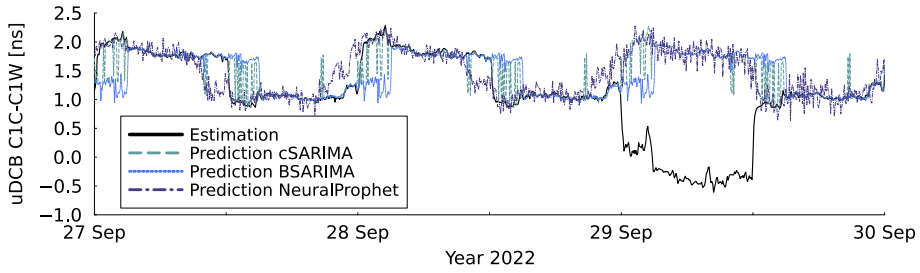


Fig. 7. Estimated and predicted C1C-C1W values for SVN73 in the period 27–30 September 2022.

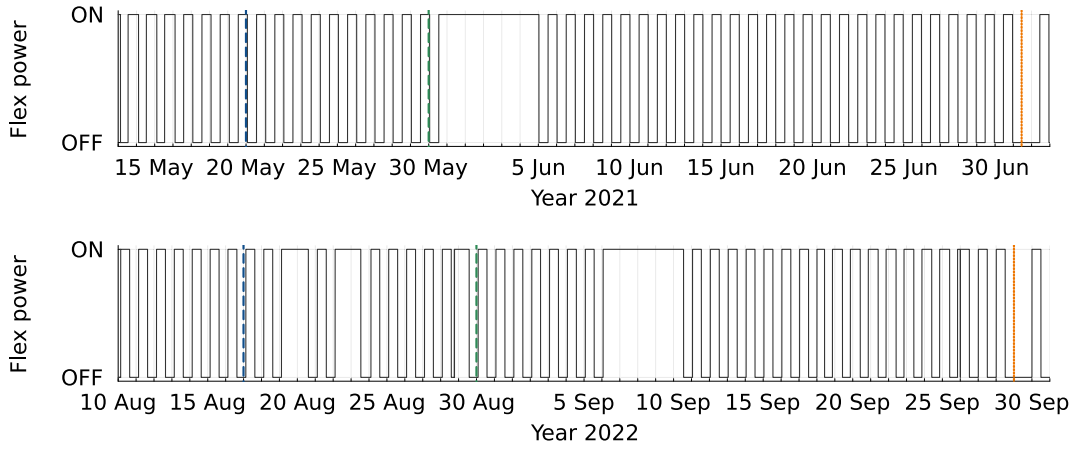


Fig. 8. Time series of flex power activation for SVN66 (top) and SVN73 (bottom). Dashed blue lines denote the end of the first training data set. Dashed green lines denote the end of the holdout data set and start of the test data set. Dotted orange lines indicate the approximate epochs of anomaly start.

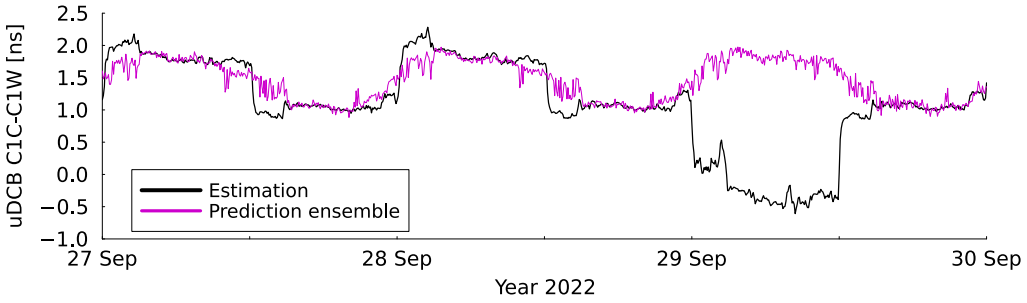


Fig. 9. Estimated and ensemble-predicted C1C-C1W values for SVN73 in the period 27–30 September 2022.

occurred to SVN66 in July 2021, several GBAS stations detected the anomaly and excluded this satellite, but WAAS monitor metrics did not trip (Phelts and Walter, 2022; Phelts et al., 2022). Although it is likely that the L1 range errors caused by this anomaly remained below the minimum WAAS error limits (Phelts et al., 2022), the uneven detection results from WAAS and GBAS monitoring systems highlight the problem of proper thresholding and binary classification for a variety of applications.

4. Monitoring strategy

Within this section, the monitoring strategy proposed in this study is presented, including the methods for scoring and probability calibration and the employed Markov chain model for the computation of epoch-wise probabilities of anomalous points. An analysis of PPP residuals of selected IGS station is shown to evaluate the impact on individual signal components and observations of the events under study. Lastly, the user perspective during these events and possible impact on high-precision and high-integrity applications is discussed.

4.1. Scoring and probability calibration

Although the computed prediction intervals in this analysis provide bounds to the values that the respective models can use for prediction, they are less useful for the task of reliable detection of anomalous signatures. One key drawback is that none of the used approaches (see Table 1)

guarantees constructing well-calibrated or optimized prediction intervals (Chen et al., 2021; Dewolf et al., 2023). Accordingly, the prediction bounds (see Eq. (8)) may fail to effectively capture a desired probability α (as a measure of detection confidence) if such bounds are used as detection thresholds. Other common strategies for anomaly detection based on prediction models rely on the computation of scores, followed by a comparison against a defined threshold (Blázquez-García et al., 2021; Schmidl et al., 2022; Boniol et al., 2024). In this case, finding an optimal threshold often requires the availability of labeled data or a representative dataset, which is less effective or unfeasible if anomalies are very rare (Cavallaro et al., 2023; Komadina et al., 2024). For both approaches, labelling a given point is a binary classification problem (i.e. anomaly present or not present), which is a less flexible approach for decision making. Alternatively, scores can be converted to calibrated probabilities, which ease the analysis of results and provides more flexibility to the classification of anomalous points. In addition, such an approach contributes to the interpretability and comparison of results obtained from different models, including ensembles (Gao and Tan 2006; Kriegel et al., 2011; Perini et al., 2021).

In this study, scores are defined as the absolute difference of predicted and estimated values

$$\chi_t = \left| \widehat{d}_t^{\,s} - \check{d}_t^{\,s} \right| \tag{14}$$

at epoch t. Assigning a probability to a score is commonly known as probability calibration. It is essentially a probabilistic classification problem (Gao and Tan, 2006; Perini et al., 2021). The goal is to estimate the probability that a score χ_t belongs to a certain class κ, including a class labelled as anomalous. Let z_κ be a binary variable which is equal to one when a given score χ_t belongs to class κ and zero if it belongs to other classes. The probability to be computed is denoted as $p(z_\kappa = 1|\chi_t)$. Due the lack of labeled examples in this study, this classification problem is solved in an unsupervised way, treating z_κ as a binary latent variable.

Provided the obtained prediction results (see Figs. 6, 7 and 9), three classes are considered in this analysis in an effort to classify all the observed variations of uDCB estimates, including the effects of changing flex power modes. These classes are henceforth referred to nominal, off-nominal and anomalous. Let $p(z_\kappa = 1) = \pi_\kappa$ be a prior probability for class κ and $p(\chi_t|\Psi_\kappa, z_\kappa = 1)$ the (sampling) probability of getting a score χ_t given a model with parameters Ψ_κ for class κ. So, the joint probability of χ_t and z_κ is expressed as $p(\chi_t, z_\kappa = 1) = \pi_\kappa p(\chi_t|\Psi_\kappa, z_\kappa = 1)$. The probability $p(\chi_t)$ of getting a score χ_t considering the $K = 3$ models parametrized by Ψ_κ, is obtained by marginalization as

$$p(\chi_t) = \sum_{\kappa=1}^{K} \pi_\kappa p(\chi_t|\Psi_\kappa, z_\kappa = 1) \tag{15}$$

which defines a mixture distribution model for the computed scores (McLachlan et al., 2019). As a reasonable selection of models for $p(\chi_t|\Psi_\kappa, z_\kappa = 1)$, scores of the nominal class ($\kappa = 1$) are assumed to be exponentially distributed, whereas off-nominal ($\kappa = 2$) and anomalous scores($\kappa = 3$) are assumed to be normally-distributed (Gao and Tan, 2006), as follows

$$\begin{aligned} p(\chi_t \,|\, \Psi_1, z_1 = 1) &= \mathrm{Exp}(\lambda) \\ p(\chi_t \,|\, \Psi_2, z_2 = 1) &= \mathcal{N}(\mu_2, \sigma_2) \\ p(\chi_t \,|\, \Psi_3, z_3 = 1) &= \mathcal{N}(\mu_3, \sigma_3) \end{aligned} \tag{16}$$

Finally, using the Bayes-Laplace rule, it follows that

$$\begin{aligned} p(z_\kappa = 1|\chi_t) &= \frac{p(\chi_t|\Psi_\kappa, z_\kappa = 1)p(z_\kappa = 1)}{p(\chi_t)} \\ &= \frac{\pi_\kappa p(\chi_t|\Psi_\kappa, z_\kappa = 1)}{\sum_{\kappa=1}^{K} \pi_\kappa p(\chi_t|\Psi_\kappa, z_\kappa = 1)} \end{aligned} \tag{17}$$

which allows to compute the probability that a given score χ_t belongs to any of the three defined classes.

A fundamental step in the described probability calibration procedure is the estimation of model parameters $\Psi = \{\lambda, \mu_2, \sigma_2, \mu_3, \varsigma_3\}$ together with the prior probabilities π_κ, defining the mixture model given by Eq. (15). For this study, this was done with the expectation–maximization algorithm (McLachlan and Krishnan, 2008; Métivier 2024) using the scores obtained from the respective holdout data sets (see Fig. 8). To account for extreme score values that (in general) are not included in a probability calibration data set, the parameter ς_3 of model $p(\chi_t|\Psi_3, z_3 = 1)$ for anomalous points was inflated by a factor η. As such, $p(\chi_t)$ denotes the probability of a given score χ_t under the model given by Eq. (15). Fig. 10 depicts the empirical tail distributions (1-eCDF) of the sampled $p(\chi_t)$ for scores in the holdout data set obtained for all the prediction models, uDCBs and satellites under analysis. For SVN66, probabilities of 10^{-2} and below are obtained for scores above 0.5 ns for almost all models and uDCBs. For SVN73, the distribution tails for C1C-C1W estimates are wider, resulting in probabilities of 10^{-1} for scores above 0.5 ns. For C2W-C2L, the obtained distributions for almost all models are similar to the ones obtained for SVN66.

4.2. Markov chain model

The probability calibration step described in the previous section is based on a fixed set of scores χ_t. As a result, high probabilities $p(z_3 = 1|\chi_t)$ may be assigned to individual outlying uDCB estimates (e.g. noisy estimates), leading to high false alarm rates for anomalous points. In addition, the obtained probabilities may not reflect effectively any existing time dependencies of uDCB estimates and corresponding scores. Based on the duration of past non-nominal signal deformation events (Shallberg et al., 2017; Phelts and Walter, 2022) and other signal deformations

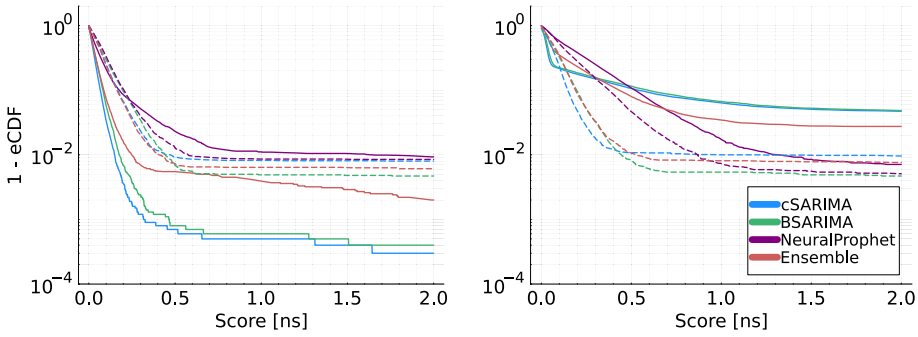


Fig. 10. Empirical tail distributions of mixture models of computed scores for SVN66 (left) and SVN73 (right). Solid and dashed lines correspond to C1C-C1W and C2W-C2L, respectively.

caused by flex power, it can be assumed that rapid changes (one to few epochs) in uDCB estimates signatures due to signal deformations are unlikely to occur.

In an effort to capture time dependencies in the computation of probabilities $p(z_\kappa = 1|\chi_t)$, a first-order Markov chain was employed for updating the values of prior probabilities π_κ at each epoch t. For this, a set of states is defined, corresponding to the three specified classes, viz. nominal, off-nominal and anomalous. At each epoch t, the vector of probabilities for each state is computed as

$$[\pi_\kappa(t)] = \Pi_{t-1}^{t}[\pi_\kappa(t-1)] \tag{18}$$

using the set of initial probabilities $\pi_\kappa(t=0)$ from probability calibration. Likewise, Π_{t-1}^{t} denotes the transition probability matrix from epoch $t-1$ to t. According to the above considerations, this matrix encodes the condition of persistent states, considering high probabilities (≥ 0.95) for transitions to the same state. Thus, at each epoch t, the computed values $p(z_\kappa = 1|\chi_{t-1}; t-1)$ from epoch $t-1$ are assigned to the latest set of priors $\pi_\kappa(t-1)$ for the computation of $\pi_\kappa(t)$ according to Eq. (18). Finally, an updated probability $p(z_\kappa = 1|\chi_t; t)$ is computed using Eq. (17).

4.3. Anomaly detection

A particular advantage of the computed epoch-wise probabilities $p(z_\kappa = 1|\chi_t; t)$ is the ease of comparison and analysis of results from a variety of detectors in a sequential manner. In this way, it is possible to determine and compare how fast a given signal anomaly can be detected. As such, in the current analysis it was opted against using a defined threshold to label a given uDCB estimate as anomalous, in an effort to generalize the presented scheme to other scenarios. Instead, time series of computed probabilities $p(z_\kappa = 1|\chi_t; t)$ are examined to quantify the level of confidence to determine that a given satellite and signal are in a nominal, off-nominal or anomalous state at epoch t, given the computed scores χ_t. For simplicity, the analysis presented in this section is focused on results for the anomalous class/state.

Fig. 11 depicts the epoch-wise probabilities of anomalous point $p(z_3 = 1|\chi_t; t)$ from all models for C1C-C1W and C2W-C2L estimates for satellite SVN66 in the period 30 May – 2 July 2021. To ease the analysis, results from the ensemble model are shown in a separate plot. As hinted by the prediction results shown in Fig. 6, all individual (and ensemble) models exhibit a very similar performance. Aside from the results on 1 July, most of the obtained values from the models lie below 10^{-2}. For C1C-C1W estimates, the permanent activation of flex power from 30 May results in probabilities above 10^{-2} in the following days until 5 June (see Fig. 8). These results depict the impact of this kind of changes in signatures of uDCB estimates, in particular if the data set used for probability calibration does not contain examples of such off-nominal changes. For C2W-C2L, probability values below 10^{-1} from all models for almost all estimates were obtained before 1 July, with only few individual points with probabilities above 1–10^{-1}, mostly attributed to estimation outliers. As flex power was permanently activated only on the L1 P(Y) signal in the period 30 May – 4 Jun, there was no impact on the obtained results for C2W-C2L.

According to the results for 1 July, probabilities of anomalous point higher than 1–10^{-3} were obtained for C1C-C1W estimates starting from 11:05 using the cSARIMA, BSARIMA and ensemble models, and from 11:20 using the NeuralProphet model. For C2W-C2L estimates, such probability levels were obtained starting from 11:10 using the cSARIMA, BSARIMA and ensemble models, and from 11:20 using the NeuralProphet model. On the other hand, probabilities of anomalous point below 1–10^{-1} were obtained after 23:00–23:05 for both sets of uDCB estimates and all models. These results suggest that the event occurred to SVN66 had a duration of approximately 12 h, starting around 11:00–11:05 UTC and having an impact on L1 and L2 signals, as also reported by Phelts et al. (2022).

Fig. 12 depicts the epoch-wise probabilities of anomalous point $p(z_3 = 1|\chi_t; t)$ from all models for C1C-C1W and C2W-C2L estimates for satellite SVN73 in the period 30 May – 30 September 2022. Before and after 29 September, most of the obtained probability values for C1C-C1W are below 10^{-2}, in particular for the results from the BSARIMA and NeuralProphet models. Other than for

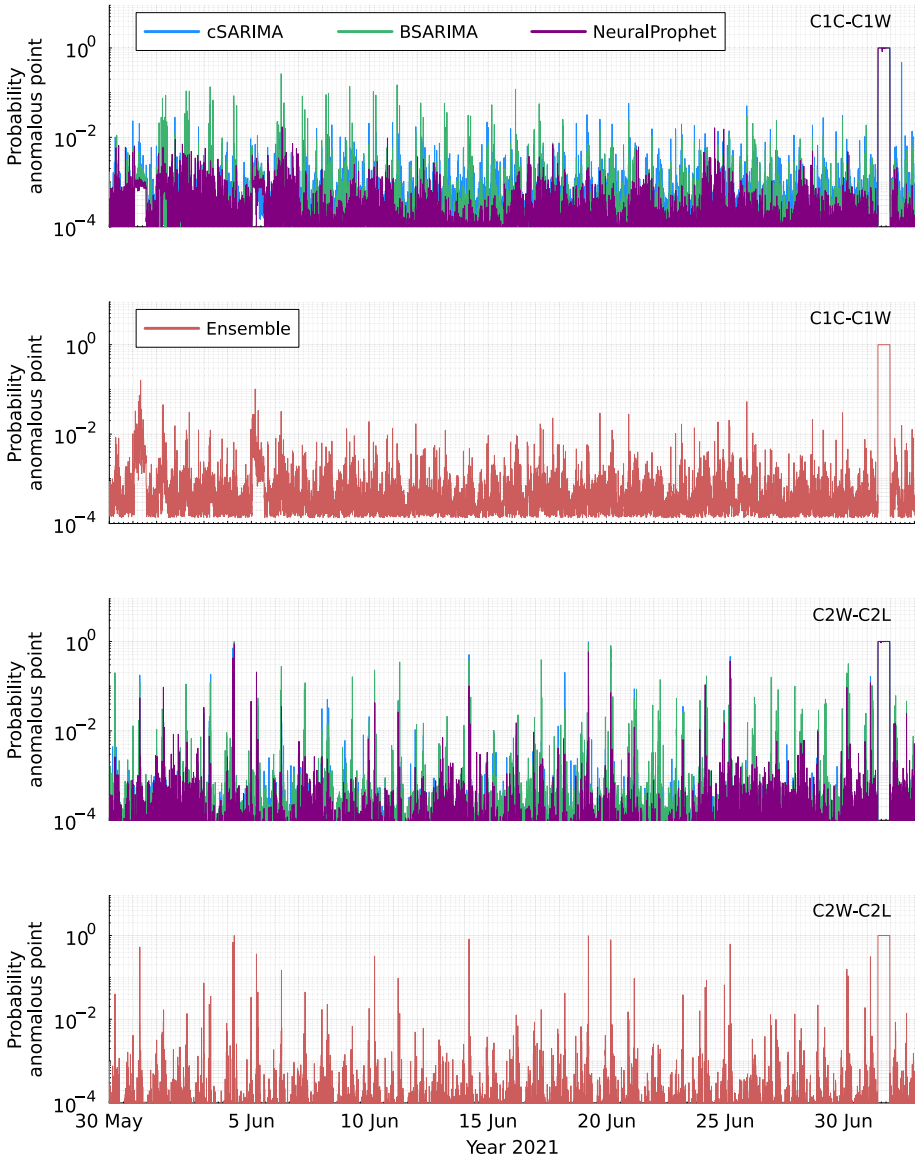


Fig. 11. Epoch-wise probability of anomalous points for SVN66 in the period 30 May – 2 Jul 2021.

SVN66, during the period of the holdout data set for probability calibration for SVN73, several changes in the activation/deactivation of flex power occurred (see Fig. 8). As a consequence, an improved fit of the distributions in the mixture model was obtained, particularly for the off-nominal examples. This allowed a better separation of the off-nominal and anomalous classes, leading to low probabilities of anomalous points even in the periods of constant changes in flex power activation/deactivation (e.g. 6–11 and 18–26 September). For C2W-C2L, probability values below 10^{-2} were obtained from all models for almost all estimates. Similar to SVN66, only few points with values above $1–10^{-1}$ were obtained, mostly attributed to estimation outliers.

As depicted in Fig. 7, off-nominal/anomalous C1C-C1W estimates were obtained from the very first minutes of 29 September. To help the analysis of results in this period, Fig. 13 shows the obtained probabilities of anomalous point from all models on 28–29 September. As expected from the obtained predictions, it can be seen that it is not possible to identify such off-nominal/anomalous estimates with high confidence during the first hours of the day using results from the cSARIMA and BSARIMA models. Only after 03:20 and 04:15, probabilities above $1–10^{-1}$ are obtained. For the case of the NeuralProphet model, probabilities above $1–10^{-1}$ are obtained starting from 00:40. Ten minutes later, the detection confidence is improved with probabilities higher than $1–10^{-2}$. Similarly, for the ensemble model, probabilities above $1–10^{-1}$ and $1–10^{-2}$ are obtained starting from 00:55 and 01:05, respectively. About two hours later, the detection confidence is increased with probabilities higher than $1–10^{-3}$, obtained

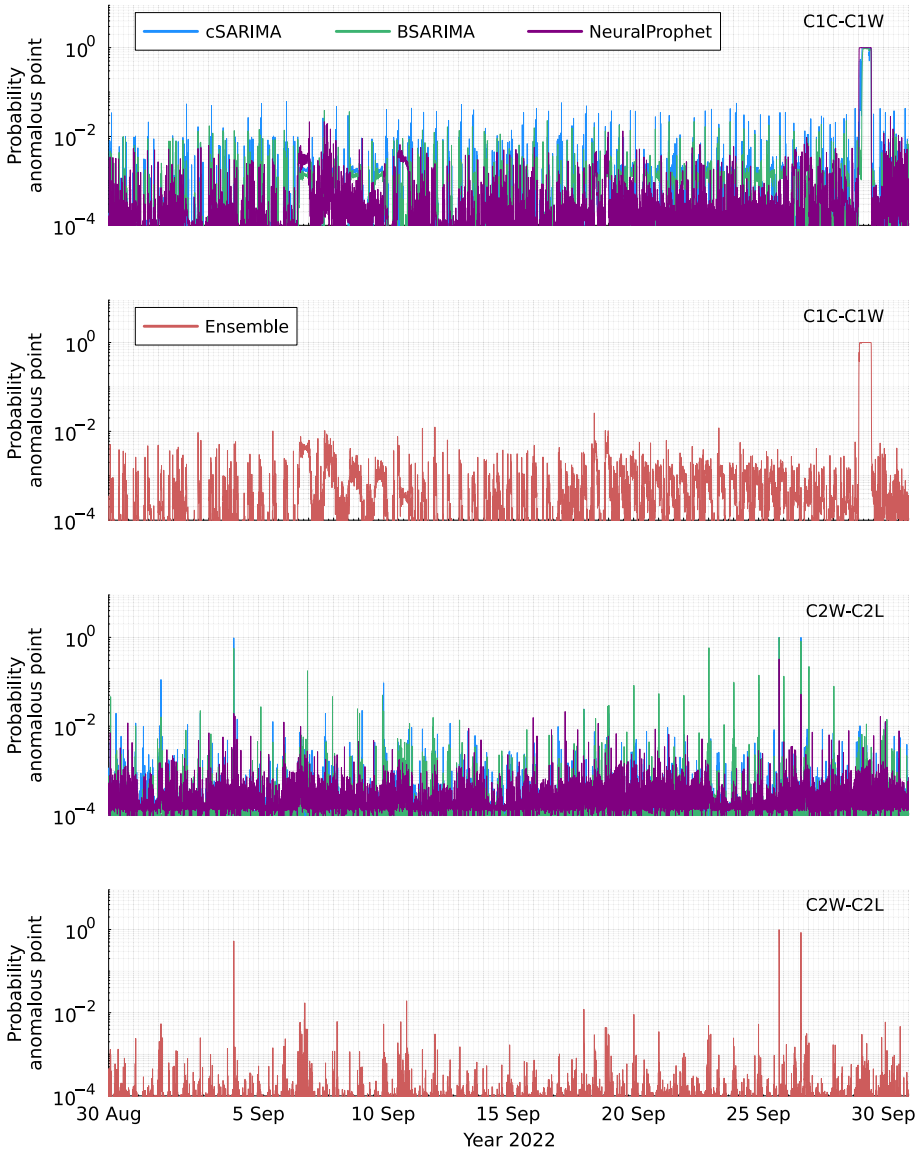


Fig. 12. Epoch-wise probability of anomalous points for SVN73 in the period 30 Aug – 30 Sep 2022.

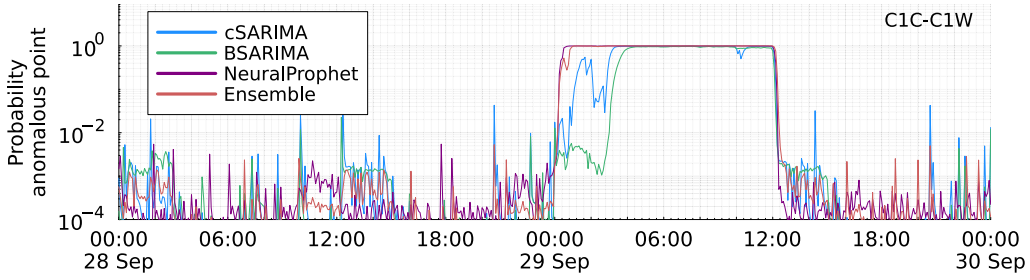


Fig. 13. Epoch-wise probability of anomalous points of C1C-C1W estimates for SVN73 in the period 29 Sep – 30 Sep 2022.

consistently for the following hours. Finally, probabilities lower than $1–10^{-1}$ were obtained after 11:55–12:05 for results from all models.

The obtained results support the early findings of previous analyses (Thoelert et al., 2023; Allende-Alba et al., 2024) and suggests the occurrence of an anomalous signal

deformation event that had an impact on (at least one) L1 signal and started during the first hour of 29 September, lasting around 12 h. Similarly, no impact on L2 signals was found in the obtained results, although from this analysis alone it cannot be completely ruled out.

4.4. PPP analysis and user perspective

According to the obtained results, the presented monitoring strategy enables the detection of signal anomalies that have an impact on code observations. However, given that DCBs are used as pseudo-observations, the specific effect of such anomalies on individual signal components and observables cannot be determined. To complement the analysis of the characteristics of the signal deformation events occurred to SVN66 and SVN73, static PPP solutions for selected IGS stations were obtained (see Table 3). Accordingly, an examination of residuals of the obtained solutions allows an assessment of the impact that such events had on individual signal components.

Two representative IGS stations for the analysis of each event were selected based on the satellite elevation at the approximate epoch of start and end of the detected anomalies. For SVN66, solutions for the HERS and BRUX stations in Hailsham, UK and Brussels, Belgium, respectively, were obtained for 30 June and 1 July 2021. In both days, the analysis was focused around epoch 11:00 UTC (i.e. at anomaly start on 1 July). The residuals of C1C, C1W and C2W observations are shown in Fig. 14. To ease the visualization, a bias of ± 1 m has been added to C1C and C2W residuals. For both stations, the residuals on 30 June do not exhibit major changes, except for an increased bias of few centimeters/decimeters for the BRUX station after 11:00. This variation aligns with the activation of flex power (see Fig. 8). On the other hand, residuals from both stations on 1 July show a noticeable change after 11:00 on all observations. For C2W, this change is sharper than for C1C and C1W. Close to end of the respective passes in both stations, the differences with respect to the period before 11:00 are at the 1 m level for C1W residuals and at the 50–60 cm level for C1C and C2W residuals. Similarly, absolute C1C-C1W residual differences after 11:00 are at the 30–40 cm level for HERS and at the 40–50 cm level for BRUX, which is roughly consistent with the obtained scores in the 1–1.3 ns range for C1C-C1W estimates during the anomaly phase (see also Fig. 6).

For the analysis of the event occurred to SVN73, solutions for the MAC1 and OUS2 stations in Macquarie Island, Australia and Dunedin, New Zealand, respectively, were obtained for 28 and 29 September 2022. In this case, the analysis was focused around epoch 12:00 UTC (i.e. at anomaly end on 29 September). The residuals of C1C, C1W and C2W observations are depicted in Fig. 15. On 28 September, no major changes in the C1C and C2W residuals are observed. For C1W, a bias increment of few centimeters is observed for both stations some minutes after 12:00, which coincides with the deactivation of flex power (see Fig. 8). On 29 September, biased C1C and C1W residuals are observed since start of tracking in both stations. In each case, C1W residuals exhibit the largest biases in this period, at the 70–80 cm level. By comparison, C1C residuals are located in the 20–30 cm range. For both stations, such biases decrease within the next half an hour after 12:00. No major changes are observed in C2W residuals in both days and stations, supporting the obtained detection results depicted in Fig. 12 for C2W-C2L estimates. During the first hours of tracking in both stations, absolute C1C-C1W residual differences reach the 50–60 cm level, roughly comparable with the obtained scores in the 2.0–2.2 ns range for C1C-C1W estimates during anomaly occurrence (see also Fig. 9).

As indicated by the obtained anomaly detection and PPP results, the event occurred to SVN66 affected (at least) C/A, L1 P(Y) and L2 P(Y) observations during approximately 12 h. Based on an analysis using WAAS measurements, Phelts and Walter (2022) reported that the likely (uncorrected) range error in C/A observations was approximately 2 m and up to 4.7 m considering the largest uncertainty in error estimation. For the case of the event occurred to SVN73, the obtained results suggest it had

Table 3
Elements of PPP solutions for selected IGS stations.

Element	Description
Type of solution	Static PPP
Precise orbit and clocks	Final products from the Center for Orbit Determination in Europe (CODE)
Observation data	IGS RINEX files (30 s) from POLARX5 receivers
Observation types	- Pseudorange: L1 C/A, L1 P(Y), L2 P(Y) - Carrier phase: L1 C/A, L2 P(Y)
estimation parameters	- Fixed station position and epoch-wise clock offsets - Slant ionospheric delays - Tropo-wet delay - Station code and phases biases - Carrier phase float ambiguities
Station/observation selection	High-elevation satellite passes

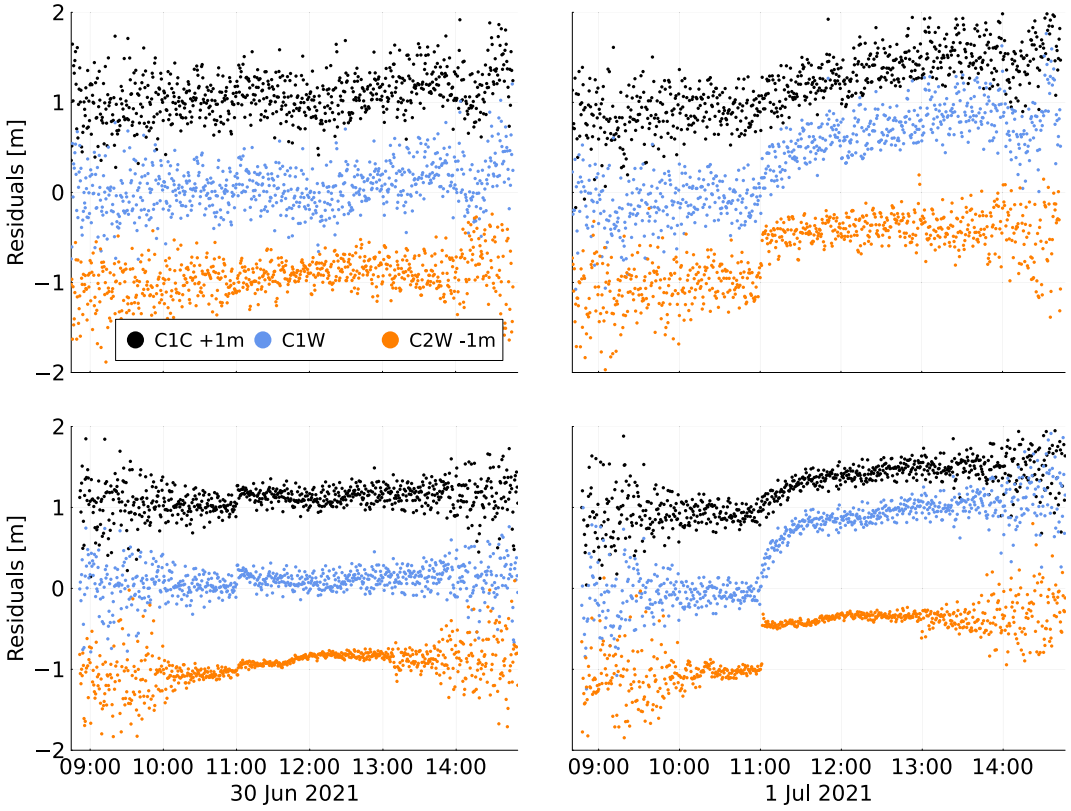


Fig. 14. Residuals of static PPP for satellite SVN66 for IGS stations HERS (top) and BRUX (bottom) on 30 June (left) and 1 July (right) 2021.

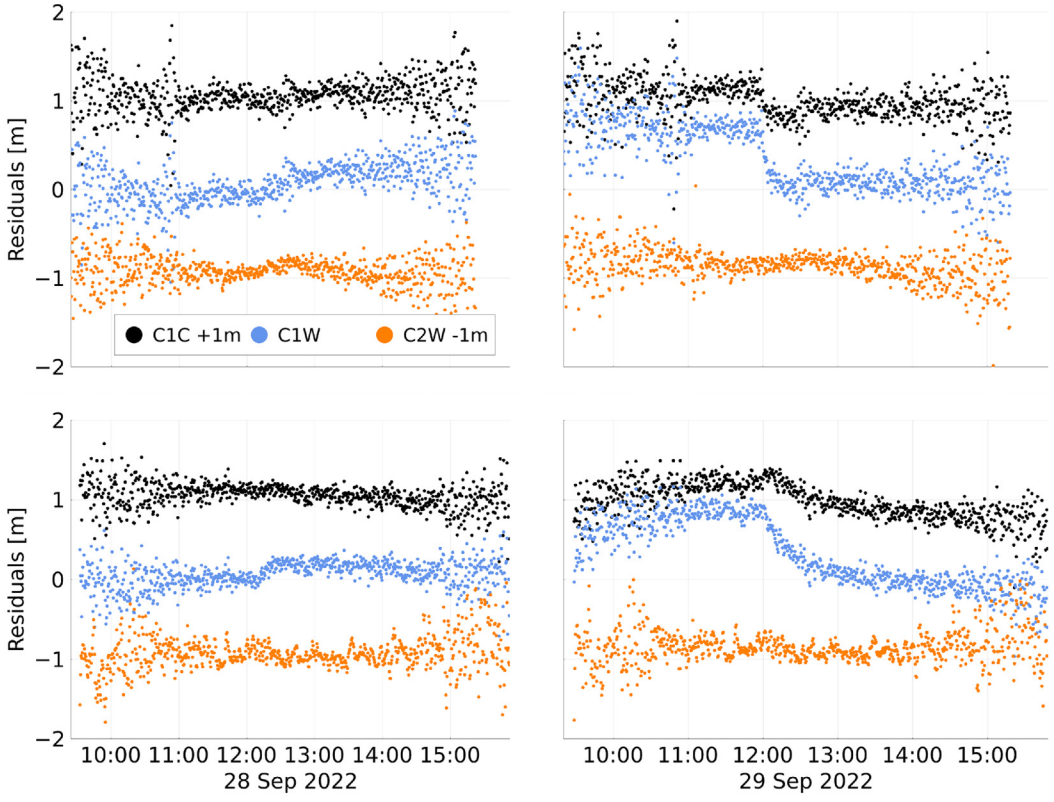


Fig. 15. Residuals of static PPP for satellite SVN73 for IGS stations MAC1 (top) and OUS2 (bottom) on 28 (left) and 29 (right) September 2022.

an impact on both L1 P(Y) and (to a lesser extent) C/A observations, also with a duration of around 12 h. Although a quantification of the resulting range errors for a variety of users is out of the scope of this study, these results also suggest the occurrence of anomalous signal distortions of slightly higher magnitude in comparison with analyzed event for SVN66, based on the impact on Septentrio PolaRx5 receivers.

Other than for aviation applications (at least for SVN66), users of C/A signals did not receive during these periods any information in broadcast navigation messages concerning both events. According to the available data from IGS navigation message files in RINEX3 (only LNAV before 2022) and RINEX4 (LNAV & CNAV starting from 2022), the transmitted timing group delays (TGD) about the L1 P(Y)-L2 P(Y) bias and inter-signal corrections (ISC) for L1 P(Y)-C/A biases did not change during anomaly occurrence with respect to values from the previous days/weeks. During both events, L1 and L2 signals from both satellites were flagged as healthy and no notice advisory to Navstar users (NANU) messages were issued (Navigation Center of the USCG, 2025). Regarding integrity information, the retrieved values of the user range accuracy (URA) from LNAV and computed non-elevation dependent integrity assured URA ($IAURA_{NED}$) from CNAV messages did not exhibit prominent changes during the occurrence of both anomalies with respect to previous days/weeks.

Although there is little indication that users of the standard positioning service (SPS) with less stringent integrity requirements were significantly impacted by the events under analysis, high-accuracy applications were likely affected, as per the obtained results from PPP processing. Even though the precision of PPP solutions is largely obtained from carrier phase observations, unmodelled or uncorrected errors in code observations (e.g. DCBs) may lead to higher convergence times and a slower integer ambiguity resolution (Kouba et al., 2017; Elsheikh et al., 2023).

5. Summary and discussion

Signal deformations have been extensively studied using observations from high-gain antennas. This approach is more suitable for the characterization of nominal signal deformations given the costly operation and limited capabilities of high-gain antennas for permanent monitoring. This paper presented a strategy for global and continuous GPS L1 and L2 signal quality monitoring, aimed at the early detection of anomalous signal deformation events. It was conceived as an integral part of a detection (using a global network of GPS receivers) plus characterization (using high-gain antennas) scheme. The proposed methodology was tested in the analysis of two recent anomalous signal deformation events occurred to SVN66 and SVN73 on 1 July 2021 and 29 September 2022, respectively.

To ensure continuous and global monitoring capabilities, the presented strategy is based on the estimation of very high-rate (unlevelled) DCBs using observations from the IGS network. These estimates were obtained epoch-wise in a satellite-per-satellite basis and used for training autoregressive models to enable a prediction-based anomaly detection scheme that is suitable for near real-time operation. Three different approaches of autoregressive models (statistical, Bayesian and neural network-based) were tested. An implicit data quality scheme for model feeding was implemented via prediction intervals. According to the obtained results, all models showed strength and weaknesses for the computation of useful predictions for anomaly detection. Overall, Bayesian models exhibited the best stability for the generation of predictions of nominal states, although a model restart may be needed for scenarios with several changes in estimates' patterns. In turn, neural network-based models showed the best flexibility to adapt to such changes and to model long-term dependencies. Based on these results, an ensemble solution was computed to improve the robustness of the scheme by harnessing the strengths of all model classes under analysis.

In an effort to tackle the problem of thresholding for anomaly detection, scores were obtained as a function of predicted and estimated values and converted to calibrated probabilities using an unsupervised learning mixture model. Epoch-wise probabilities of anomalous points were computed by using a Markov chain model. One advantage of the proposed strategy is its flexibility for the analysis of results. The computed epoch-wise probabilities are easier to interpret and compare considering results from different models. As such, the obtained probabilities quantify the confidence of detection, which increases with time in case of an actual anomaly, as more evidence is gathered.

The obtained results suggest that the proposed methodology is suitable for a prompt identification of anomalous signal deformation events on L1 and L2 on a global scale. Although the amount of data and the sparseness of anomalies under analysis make difficult to formulate a general statement about the detection capabilities of the presented scheme, the obtained mixture models (Fig. 10) provide some hints. For instance, under the mixture model of the ensemble solution, scores of 0.5 ns exhibit probabilities well below 10^{-1} for all cases under analysis. Likewise, in terms of probabilities of anomalous points using results from the ensemble solution, the event occurred to SVN66 could be detected through the impact on C1C-C1W and C2W-C2L estimates with probability values higher than $1–10^{-3}$ within the first 10 min after anomaly start. For the event occurred to SVN73, the detection was done through the impact on C1C-C1W estimates with probability values higher than $1–10^{-2}$ within the first hour after anomaly start. Similarly, in a complementary analysis using results from static PPP solutions from selected IGS stations, it was possible to identify that the event occurred to SVN66 had an impact on at least C/A, L1 P(Y) and L2 P(Y) signals. For the case

of SVN73, the event apparently affected C/A and L1 P(Y) signals only.

Given that the proposed monitoring system is not application-specific, it is capable of identifying small or short-lived anomalies that may not be detectable by specialized networks, like SBAS or GBAS. In this way, the presented methodology aims at contributing for a better understanding and characterization of errors that are relevant for future applications with stringent requirements in both accuracy and integrity.

Declaration of competing interest

The authors declare that they have no known competing financial interests or personal relationships that could have appeared to influence the work reported in this paper.

Acknowledgments

The authors are grateful to Peter Steigenberger (DLR/GSOC) for computing 2 h-DCB estimates used as reference for evaluation of very high-rate uDCBs. This study makes use of broadcast ephemeris and observation data from the International GNSS Service. The support of all the involved institutions and analysis centers is thankfully acknowledged.

References

Akos, D.M., Phelts, R.E., Pullen, S., Enge, P., 2000. Signal quality monitoring: test results. In: Proc. of the National Technical Meeting of The Institute of Navigation, Anaheim, CA, pp. 536–541.

Allende-Alba, G., Thölert, S., Steigenberger, P., Meurer, M., 2024. Catalogue of GNSS signal anomalies using high-rate differential code bias estimates. In: Proc. of the International Technical Meeting of the Satellite Division of The Institute of Navigation, Long Beach, CA. pp. 241–257. https://doi.org/10.33012/2024.19490.

Audibert, J., Michiardi, P., Guyard, F., Marti, S., Zuluaga, M.A., 2022. Do deep neural networks contribute to multivariate time series anomaly detection? Pattern Recogn. 132. https://doi.org/10.1016/j.patcog.2022.108945.

Banville, S., Langley, R.B., 2011. Defining the basis of an integer-levelling procedure for estimating slant total electron content. In: Proc. of the International Technical Meeting of the Satellite Division of The Institute of Navigation, Portland, OR, p. 2542.

Blázquez-García, A., Conde, A., Mori, U., Lozano, J.A., 2021. A review on outlier/anomaly detection in time series data. ACM Comput. Surv. 54 (3), 1–33. https://doi.org/10.1145/3444690.

Boniol, P., Liu, Q., Huang, M., Palpanas, T., Paparrizos, P., 2024. Dive into time-series anomaly detection: a decade review. Preprint arXiv:2412.20512.

Box, G.E.P., Jenkins, G.M., 1970. Time Series Analysis: Forecasting and Control, 1st ed. University of Michigan.

Brockwell, P.J., Davis, R.A., 2016. Introduction to time series and forecasting, 3rd ed. Springer, New York.

Cavallaro, C., Cutello, V., Pavone, M., Zito, F., 2023. Discovering anomalies in big data: a review focused on the application of metaheuristics and machine learning techniques. Front. Big Data 6. https://doi.org/10.3389/fdata.2023.1179625 1179625.

Chandola, V., Banerjee, A., Kumar, V., 2009. Anomaly detection: a survey. ACM Comput. Surv. 41 (3). https://doi.org/10.1145/1541880.1541882.

Chen, H., Huang, Z., Lam, H., Qian, H., Zhang, H., 2021. Learning prediction intervals for regression: generalization and calibration. In: Proc. of the 24Th International Conference on Artificial Intelligence and Statistics, PMLR 130, pp. 820–828.

Deng, Y., Guo, F., Ren, X., Ma, F., Zhang, X., 2021. Estimation and analysis of multi-GNSS observable-specific code biases. GPS Solut. 25, 100. https://doi.org/10.1007/s10291-021-01139-6.

Dewolf, N., Baets, B.D., Waegemann, W., 2023. Valid prediction intervals for regression problems. Artif. Intell. Rev. 56, 577–613. https://doi.org/10.1007/s10462-022-10178-5.

Edgar, C., Czopek, F., Barker, B., 1999. A cooperative anomaly resolution on PRN-19. In: Proc. of the 12Th International Technical Meeting of the Satellite Division of the Institute of Navigation, Nashville, TN, pp. 2269–12268.

Elsheikh, M., Iqbal, U., Noureldin, A., Korenberg, M., 2023. The implementation of precise point positioning (PPP): a comprehensive review. Sensors 23, 8874. https://doi.org/10.3390/s23218874.

Esenbuğa, Ö.G., Hauschild, A., 2020. Impact of flex power on GPS block IIF differential code biases. GPS Solut. 24, 91. https://doi.org/10.1007/s10291-020-00996-x.

Esenbuğa, Ö.G., Hauschild, A., Steigenberber, P., 2023. Recent flex power changes. GPS Solut. 27, 104. https://doi.org/10.1007/s10291-023-01415-7.

Fernández, A., García, S., Galar, M., Prati, R.C., Krawczyk, B., Herrera, F., 2018. Learning From Imbalanced Data Sets. Springer Cham.

Fjelde, T.E., Xu, K., Widmann, D., Tarek, M., Pfiffer, C., Trapp, M., Axen, S.D., Sun, X., Hauru, M., Yong, P., Tebutt, W., Ghahramani, Z., Ge, H., 2025. Turing.jl: a general-purpose probabilistic programming language. In: ACM Transactions on Probabilistic Machine Learning. https://doi.org/10.1145/371189.

Gao, J., Tan, P., 2006. Converting output scores from outlier detection algorithms into probability estimates. In: Proc. of the IEEE International Conference on Data Mining, Hong Kong, China. pp. 212–221. https://doi.org/10.1109/ICDM.2006.43.

Ge, H., Xu, K., Ghahramani, Z., 2018. Turing: a language for flexible probabilistic inference. In: Proc. of the International Conference on Artificial Intelligence and Statistics, Lanzarote, Spain. pp. 1682–1690. https://doi.org/10.17863/CAM.42246.

Gong, X., Lou, Y., Zheng, F., Gu, S., Shi, C., Liu, J., Jing, G., 2018. Evaluation of calibration of BeiDou receiver-related pseudorange biases. GPS Solut. 22, 98. https://doi.org/10.1007/s10291-018-0765-3.

Gong, X., Gu, S., Zheng, F., Wu, Q., Liu, S., Lou, Y., 2021. Improving GPS and Galileo precise data processing based on calibration of signal distortion biases. Measurement 174. https://doi.org/10.1016/j.measurement.2021.108981.

Gong, X., Zheng, F., Gu, S., Zhang, Z., Lou, Y., 2022. The long-term characteristics of GNSS signal distortion biases and their empirical corrections. GPS Solut. 26, 52. https://doi.org/10.1007/s10291-022-01238-y.

Gupta, M., Gao, J., Aggarwal, C., Han, J., 2014. Outlier detection for temporal data. Synthesis Lectures on Data Mining and Knowledge Discovery. Springer Nature, Switzerland.

Hyndman, R.J., Athanasopoulos, G., 2021. Forecasting: principles and practice, 3rd ed. OTexts.

Koenker, R., Bassett, G., 1978. Regression quantiles. Econometrica 46 (1), 33–50. https://doi.org/10.2307/1913643.

Komadina, A., Martinić, M., Groš, S., Mihajlović, Ž., 2024. Comparing threshold selection methods for network anomaly detection. IEEE Access 12, 124943–124973. https://doi.org/10.1109/ACCESS.2024.3452168.

Kontopoulou, V., Panagopoulos, A.D., Kakkos, I., Matsopoulos, G.K., 2023. A review of ARIMA vs machine learning approaches for time series forecasting in data driven networks. Future Internet 15 (8), 255. https://doi.org/10.3390/fi15080255.

Kriegel, H.P., Kroger, P., Schubert, E., Zimek, A., 2011. Interpreting and unifying outlier scores. In: Proc. of the SIAM International Conference on Data Mining, Phoenix, AZ. https://doi.org/10.1137/1.9781611972818.2.

Lou, Y., Zhang, Z., Gong, X., Zheng, F., Gu, S., Shi, C., 2023. Estimating GPS satellite and receiver differential code bias based on signal distortion bias calibration. GPS Solut. 27, 48. https://doi.org/10.1007/s10291-022-01388-z.

Hauschild, A., 2017. Basic observation equations. In: Teunissen, P.J.G., Montenbruck, O. (Eds.), Springer Handbook of Global Navigation Satellite System. Springer International, pp. 561–582.

Hauschild, A., Montenbruck, O., 2016. A study on the dependency of GNSS pseudorange biases on correlator spacing. GPS Solut. 20, 159–171. https://doi.org/10.1007/s10291-014-0426-0.

He, H., Garcia, E.A., 2009. Learning from imbalanced data. IEEE Trans. Knowl. Data Eng. 21 (9), 1263–1284. https://doi.org/10.1109/TKDE.2008.239.

Hegarty, C.J., Powers, E.D., Fonville, B., 2005. Accounting for timing biases between GPS, modernized GPS, and GALILEO signals. In: Proc. of the ION GNSS, Institute of Navigation, Long Beach, CA. pp. 2401–2407.

Hoffman, M.D., Gelman, A., 2014. The No-U-turn sampler: adaptively setting path lengths in Hamiltonian Monte Carlo. J. Mach. Learn. Res. 15 (47), 1593–1623. https://doi.org/10.5555/2627435.2638586.

Håkansson, M., Jensen, A.B.O., Horemuz, M., Hedling, G., 2016. Review of code and phase biases in multi-GNSS positioning. GPS Solut. 21 (3), 849–860. https://doi.org/10.1007/s10291-016-0572-7.

Hyndman, R.J., Khandakar, Y., 2008. Automatic time series forecasting: the forecast package for R. J. Stat. Softw. 27 (3), 1–22. https://doi.org/10.18637/jss.v027.i03.

IGS/RTCM RINEX Committee Chair, 2024. The receiver independent exchange format, version 4.02. Available online https://files.igs.org/pub/data/format/rinex_4.02.pdf.

Johnston, G., Riddell, A., Hausler, G., 2017. The international GNSS Service. In: Teunissen, P.J.G., Montenbruck, O. (Eds.), Springer Handbook of Global Navigation Satellite System. Springer International, pp. 967–982.

Lestarquit, L., Gregoire, Y., Thevenon, P., 2012. Characterising the GNSS correlation function using a high-gain antenna and long coherent integration – application to signal quality monitoring. In: Myrtle Beach, S.C. (Ed.), Proc. of the Institute of Electrical and Electronics Engineers/institute of Navigation PLANS, Myrtle Beach, SC, pp. 307–316.

Li, Z., Yuan, Y., Li, H., Ou, J., Huo, X., 2012. Two-step method for the determination of the differential code biases of COMPASS satellites. J. Geod. 86 (11), 1059–1076. https://doi.org/10.1007/s00190-012-0565-4.

Kouba, J., Lahaye, F., Tétreault, P., 2017. Precise Point Positioning. In: Teunissen, P.J.G., Montenbruck, O. (Eds.), Springer Handbook of Global Navigation Satellite System. Springer International, pp. 723–752.

Mannucci, A.J., Wilson, B.D., Yuan, D.N., Ho, C.G., Lindqwister, U.J., Runge, T.F., 1998. A global mapping technique for GPS-derived ionospheric total electron content measurements. Radio Sci. 33 (3), 565–582. https://doi.org/10.1029/97RS02707.

McLachlan, G.J., Krishnan, T., 2008. The EM algorithm and extensions. Wiley Series in Probability and Statistics, 2nd Edition.

McLachlan, G.J., Lee, S.X., Rathnayake, S.I., 2019. Finite mixture models. Ann. Rev. Statist. Its Appl. 6, 355–378. https://doi.org/10.1146/annurev-statistics-031017-100325.

Métivier, D., 2024. ExpectationMaximization.jl: A simple but generic implementation of Expectation Maximization algorithms to fit mixture models. Url: hal.inrae.fr/hal-04784091. doi: hal-04784091.

Mitelman, A.M., Phelts, E., Akos, D., Pullen, S., Enge, P., 2004. Signal deformations on nominally healthy GPS satellites. In: Proc. of the National Technical Meeting of The Institute of Navigation, San Diego, CA.

Mitelman, A.M., 2005. Signal quality monitoring for GPS augmentation systems. PhD Thesis, Stanford University. ISBN: 9780493383132.

Montenbruck, O., Hauschild, A., Steigenberger, P., 2014. Differential code bias estimation using multi-GNSS observations and global ionosphere maps. Navigation 61 (3), 191–201. https://doi.org/10.1002/navi.64.

Montenbruck, O. et al., 2017. The multi-GNSS experiment (MGEX) of the international GNSS service (IGS) – achievements, prospects and challenges. Adv. Space Res. 59 (7), 1671–1697. https://doi.org/10.1016/j.asr.2017.01.011.

Navigation Center of the USCG, 2025. Archives of the Navigation Center of the United States Coast Guard. U.S. Department of Homeland Security. navcen.uscg.gov/archives.

Negrinho, A., Fernandes, P., Boto, P., Nunes, F., Sousa, F., 2021. Evil waveforms detection solutions for autonomous navigation integrity. In: Proc. of the 34th International Technical Meeting of the Satellite Division of The Institute of Navigation, St. Louis, MO, pp. 4097–4115.

Pagot, J.B., Thevenon, P., Julien, O., Gregoire, Y., Amarillo-Fernandez, F., Maillard, D., 2015. Estimation of GNSS signals' nominal distortions from correlator and chip domain. In: Dana Point, C.A. (Ed.), Proc. of the International Technical Meeting of Satellite Division of the Institute of Navigation, Dana Point, CA, pp. 415–427.

Paparrizos, J., Kang, Y., Boniol, P., Tsay, R.S., Palpanas, T., Franklin, M.J., 2022. TSB-UAD: an end-to-end benchmark suite for univariate time-series anomaly detection. Proc. of the VLDB Endowment 15 (8), 1697–1711. https://doi.org/10.14778/3529337.3529354.

Patcha, A., Park, J.M., 2007. An overview of anomaly detection techniques: existing solutions and latest technological trends. Comput. Netw. 51 (12), 3448–3470. https://doi.org/10.1016/j.comnet.2007.02.001.

Perini, L., Vercruyssen, V., Davis, J., 2021. Quantifying the confidence of anomaly detectors in their example-wise predictions. In: Hutter, F., Kersting, K., Lijffijt, J., Valera, I. (Eds.), Machine Learning and Knowledge Discovery in Databases. Lecture Notes in Computer Science 12459. https://doi.org/10.1007/978-3-030-67664-3_14.

Phelts, R.E., 2001. Multicorrelator techniques for robust mitigation of threats to GPS signal quality. PhD Thesis, Stanford University. ISBN: 9780493383132.

Phelts, R.E., Akos, D., Enge, P., 2000. Robust signal quality monitoring and detection of evil waveforms. In: Proc. of the 13th International Technical Meeting of Satellite Division of The Institute of Navigation, Salt Lake City, UT. pp. 1180–1190.

Phelts, R.E., Akos, D.M., 2006. Effects of signal deformation on modernized GNSS signals. J. Global Posit. Syst. 5 (1), 2–10. https://doi.org/10.5081/jgps.5.1.2.

Phelts, R.E., Walter, T., Enge, P., 2009. Characterizing nominal analog signal deformation on GNSS signals. In: Proc. of the 22nd International Technical Meeting of Satellite Division of the Institute of Navigation, Savannah, GA, pp. 1343–1350.

Phelts, R.E., Wong, G., Walter, T., Enge, P., 2013. Signal deformation monitoring for dual-frequency WAAS. In: Proc. of the International Technical Meeting of The Institute of Navigation, San Diego, CA. pp. 93–106.

Phelts, E.R., Walter, T., 2022. Characterizing GPS signal deformations using the WAAS signal quality monitor. In: Proc. of the International Technical Meeting of the Institute of Navigation. https://doi.org/10.33012/2022.18304.

Phelts, E.R., Walter, T., Sanchez, R., 2022. Nominal GPS signal deformations: 10 years of WAAS signal quality monitoring. In: Proc. of the International Technical Meeting of The Institute of Navigation, Long Beach, CA, 374-388. https://doi.org/10.33012/2022.18257.

Rewicki, F., Denzier, J., Niebling, J., 2023. Is it worth it? Comparing six deep and classical methods for unsupervised anomaly detection in time series. Appl. Sci. 13 (3), 1778. https://doi.org/10.3390/app13031778.

Schmidl, S., Wenig, P., Papenbrock, T., 2022. Anomaly detection in time series: a comprehensive evaluation. Proc. of the VLDB Endowment 15 (9), 1779–1797. https://doi.org/10.14778/3538598.3538602.

Shallberg, K.W., Ericson, S.D., Phelts, E.R., Walter, T., Kovach, K., Altshuler, E., 2017. Catalog and description of GPS and WAAS L1 C/A signal deformation events. In: Proc. of the International Technical Meeting of the Institute of Navigation, Monterey, CA, pp. 508–520. https://doi.org/10.33012/2017.14877.

Steigenberger, P., Thölert, S., Montenbruck, O., 2019. Flex power on GPS Block IIR-M and IIF. GPS Solut. 23, 8. https://doi.org/10.1007/s10291-018-0797-8.

Song, J., Milner, C., Selmi, I., 2020. Signal deformation fault monitors for dual-frequency GBAS. Navigation 67 (2), 379–396. https://doi.org/10.1002/navi.360.

Su, K., Jiao, G., 2023a. Two modified multi-frequency GNSS approaches to estimate the pseudorange observable-specific signal bias for the CDMA and FDMA models. GPS Solut. 27, 83. https://doi.org/10.1007/s10291-023-01417-5.

Su, K., Jiao, G., 2023b. Estimation of BDS pseudorange biases with high temporal resolution: feasibility, affecting factors, and necessity. Satell. Navig. 4, 17. https://doi.org/10.1186/s43020-023-00103-8.

Taylor, S.J., Letham, B., 2018. Forecasting at scale. Am. Stat. 72 (1), 37–45. https://doi.org/10.1080/00031305.2017.1380080.

Triebe, O., Laptev, N., Rajagopal, R., 2019. AR-Net: a simple auto-regressive neural network for time-series. Preprint arXiV 1911, 12436.

Triebe, O., Hewamalage, H., Pilyugina, P., Laptev, N., Bergmeir, C., Rajagopal, R., 2021. NeuralProphet: explainable forecasting at scale. Preprint arXiv:2111.15397.

Thevenon, P., Tessier, Q., Maillard, D., Cabantous, M., Amarillo-Fernández, F., De Oliveira Salgueiro, F., Julien, O., 2014. Detection performances of evil waveforms monitors for the GPS L5 signal. In: Proc. of the 27Th International Technical Meeting of the Satellite Division of the Institute of Navigation, Tampa, FL, pp. 3312–3322.

Thoelert, S., Enneking, C., Vergara, M., Sgammini, M., Antreich, F., Meurer, M., Brocard, D., Rodriguez, C., 2015. GNSS nominal signal distortions – estimation, validation and impact on receiver performance. In: Proc. of the International Technical Meeting of the Institute of Navigation, Tampa, FL, pp. 1902–1923.

Thoelert, S., Antreich, F., Enneking, C., 2019. Meurer, M (2019) BeiDou 3 signal quality analysis and its impact on users. Navigation 66, 295–704. https://doi.org/10.1002/navi.331.

Thoelert, S., Circiu, M.S., Meurer, M., 2020. Impact of satellite biases on the position in differential MFMC applications. In: Proc. of the International Technical Meeting of the Institute of Navigation, San Diego, CA. pp. 222–235.

Thoelert, S., Allende-Alba, G., Steigenberger, P., 2023. GNSS signal anomaly detection using DCB estimates and machine learning algorithms. Presented at the ION GNSS+ meeting, September 11-15 Denver CO.

Vergara, M., Antreich, F., Enneking, C., Sgammini, M., Seco-Granados, G., 2020. A model for assessing the impact of linear and nonlinear distortions on a GNSS receiver. GPS Solut. 24, 5. https://doi.org/10.1007/s10291-019-0917-0.

Villiger, A., Schaer, S., Dach, R., Prange, L., Sušnik, A., Jäggi, A., 2019. Determination of GNSS pseudo-absolute code biases and their long-term combination. J. Geod. 93, 1487–1500. https://doi.org/10.1007/s00190-019-01262-w.

Wang, N., Yuan, Y., Li, Z., Montenbruck, O., Tan, B., 2016. Determination of differential code biases with multi-GNSS observations. J. Geod. 90 (3), 209–228. https://doi.org/10.1007/s00190-015-0867-4.

Wang, N., Li, Z., Duan, B., Hugentobler, U., Wang, L., 2020. GPS and GLONASS observable-specific code bias estimation: comparison of solutions from the IGS and MGEX networks. J. Geod. 94, 74. https://doi.org/10.1007/s00190-020-01404-5.

West, M., Harrison, J., 1997. Bayesian Forecasting and Dynamic Models. Springer Science+Business Media, New York.

Wireman, M., Gunawardena, S., Carroll, M., 2017. High-fidelity signal deformation analysis of the live sky GLONASS constellation using chip shape processing. Proc. of the International Technical Meeting of the Institute of Navigation, Monterey, CA.

Wong, G., Phelts, R.E., Walter, T., Enge, P., 2011. Alternative characterization of analog signal deformation for GNSS-GPS satellites. In: Proc. of the International Technical Meeting of The Institute of Navigation, San Diego, CA. pp. 497–507.

Woo, K.T., 2000. Optimum semicodeless carrier-phase tracking of L2. Navigation 47 (2), 82–99. https://doi.org/10.1002/j.2161-4296.2000.tb00204.x.

Wu, R., Keogh, E.J., 2023. Current time series anomaly detection benchmarks are flawed and are creating the illusion of progress. IEEE Trans. Knowl. Data Eng. 35, 2421–2429. https://doi.org/10.1109/TKDE.2021.3112126.

Wu, Z., Li, S., Wan, H., Ji, M., Mao, P., Xiong, S., 2024. Effects of BDS flex power on DCB estimation and PPP convergence. GPS Solut. 28, 41. https://doi.org/10.1007/s10291-023-01581-8.

Xiang, Y., Xu, Z., Gao, Y., Yu, W., 2020. Understanding long-term variations in GPS differential code biases. GPS Solut. 24, 118. https://doi.org/10.1007/s10291-020-01034-6.

Yang, X., Liu, W., Huang, J., Xiao, W., Wang, F., 2022. Real-time monitoring of GPS flex power based on machine learning. GPS Solut. 26, 73. https://doi.org/10.1007/s10291-022-01257-9.

Zamanzadeh Darban, Z., Webb, G.I., Pan, S., Aggarwal, C., Salehi, M., 2024. Deep learning for time series anomaly detection: a survey. ACM Comput. Surv. 57 (1), 1–42. https://doi.org/10.1145/3691338.

Zhang, B., Teunissen, P.J.G., Yuan, Y., Zhang, X., Li, M., 2019. A modified carrier-to-code leveling method for retrieving ionospheric observables and detecting short-term temporal variability of receiver differential code biases. J. Geod. 93, 19–28. https://doi.org/10.1007/s00190-018-1135-1.

Zhuang, C., Zhao, H., Sun, C., Feng, W., 2020. Detection and classification of GNSS signal distortions based on quadratic discriminant analysis. IEEE Access 8, 25221–25236. https://doi.org/10.1109/ACCESS.2020.2965617.